minerals

MDPI

Article

Geochemical Constraints on Petrogenesis and Tectonics of the Middle Devonian Granitic and Coeval Mafic Magmatism from the Tannuola Terrane (Northern Central Asian Orogenic Belt)

Evgeny V. Vetrov [1,2,*], Evgeny A. Pikhutin [1,2] and Natalia I. Vetrova [1]

[1] Sobolev Institute of Geology and Mineralogy, Koptyuga Ave. 3, 630090 Novosibirsk, Russia
[2] Siberian Research Institute of Geology, Geophysics and Mineral Resources, Krasny Prospect, 67, 630091 Novosibirsk, Russia
* Correspondence: vetrov@igm.nsc.ru

Highlights:

- Middle Devonian zircon U-Pb crystallization age is found in the Tannuola terrane.
- The peralkaline A-type granites and coeval mafic rocks record the intraplate extensional setting.
- The granitic rocks have positive (+5.6 to +6.2) εNd(t) values and Ediacaran–Early Cambrian model ages.
- The geodynamic model is mantle plume activity beneath northern Central Asian Orogenic Belt areas during the Givetian period.

Abstract: The Tannuola terrane, located in the northern Central Asian Orogenic Belt, comprises magmatic rocks, attributed to island-arc and collisional settings during the Early Cambrian to the Late Ordovician. However, zircon U-Pb age, geochemical, and Sr-Nd isotopic constraints demonstrate that there was a short episode of peralkaline A-type granite magmatism in the northeast border area of the Tannuola terrane. The obtained zircon U-Pb age of 387.7 ± 3.3 Ma indicates emplacement of the peralkaline A-type granitic rocks in the Middle Devonian (Eifelian–Givetian period boundary). Petrologically, these rocks are mainly composed of riebeckite granites and aplites, which are approximately synchronous with augite-rich dolerites. The granitic rocks are ferroan and calc-alkalic to alkali-calcic in composition. They are characterized by a high content of SiO_2, total alkali, Zr, and total REE. Significant depletion of Ba, Sr, P, Ti, and Eu indicates fractionation of plagioclase and/or K-feldspar. The values of εNd(t) in riebeckite granites range from +5.61 to +6.55, and the calculated two-stage model age ranges between 610 and 520 Ma. Coeval dolerites on the chondrite-normalized REE pattern, $(Th/Yb)_{pm}$–$(Nb/Yb)_{pm}$, and Th/Yb–Nb/Yb diagrams show compositional affinity between E-MORB and OIB. They are rich in incompatible elements with high HFSE/LREE ratios (Nb/La > 1), indicating that the primary magma originated from the lithospheric mantle metasomatized by asthenosphere-derived melt. Based on these geochemical characteristics, it can be reasonably inferred that the peralkaline A-type granitic rocks, and the coeval mafic rocks, are anorogenic and were emplaced in an extensional tectonic environment despite slightly higher Y/Nb values, which might be caused by a crustal contamination effect. The geochemistry of mafic rocks suggests that the magma originated from the enriched mantle sources. The results of a zircon-saturation thermometer show high initial magma temperatures between 923 and 1184 °C, with an average of 1030 °C, indicating this rock association might be related to a mantle plume beneath the northern Central Asian Orogenic Belt.

Keywords: Devonian; peralkaline; A-type granite; anorogenic environment; mantle plume; Central Asian Orogenic Belt

Citation: Vetrov, E.V.; Pikhutin, E.A.; Vetrova, N.I. Geochemical Constraints on Petrogenesis and Tectonics of the Middle Devonian Granitic and Coeval Mafic Magmatism from the Tannuola Terrane (Northern Central Asian Orogenic Belt). *Minerals* **2022**, *12*, 1282. https://doi.org/10.3390/min12101282

Academic Editor: Federica Zaccarini

Received: 16 September 2022
Accepted: 9 October 2022
Published: 12 October 2022

1. Introduction

In recent decades, peralkaline A-type granites attracted strong interest in the geological community because of their economically significant mineralization. For instance, these granites may contain mineralization of rare metals (such as Ta and Nb) that are indispensable for the modern economy [1,2]. Therefore, studying their petrogenesis and tectonic environments is important for understanding the continental lithospheric evolution, as well as providing genetic models for economic potential estimation on universal or local scales. Modern knowledge allows us to suggest that the evolution of the peralkaline A-type magmas occurred in extensional intraplate or post-orogenic environments associated with alkaline-type mafic rocks [3–5]. Nevertheless, there is still no consensus on their origin. Peralkaline A-type granitic rocks display differing sources involved in their genesis, magmatic evolution processes, and environment conditions [6–8].

The Central Asian Orogenic Belt is the tectonic collage of microcontinents and terranes of various tectonic affinity located between the European, Siberian, Tarim, and North China cratons [9,10]. Its crustal growth was represented by lateral amalgamation of different terranes and microcontinents [11,12], as well as the substantial vertical addition of juvenile material derived from the upper mantle [13]. Granitic and mafic rocks cover a vast area of central Asia, so their comprehensive study provides critical information on the significant growth of the continental crust and places important constraints on the tectonic evolution of the Central Asian Orogenic Belt. The Central Asian Orogenic Belt is characterized by a vast distribution of the Paleozoic and the Mesozoic peralkaline granitic intrusions (Figure 1e) [14–16]. This study focuses on the peralkaline A-type granites from the Tannuola terrane in the northern part of the Central Asian Orogenic Belt. We present results of whole-rock major and trace elements, Sr-Nd isotopic compositions, and the zircon U–Pb ages in an attempt to constrain the timing of the emplacement and to reconstruct the petrogenetic evolution, magma sources, and tectonic setting of the peralkaline A-type granitic rocks from the Tannuola terrane within the framework of the geodynamic evolution of the Central Asian Orogenic Belt.

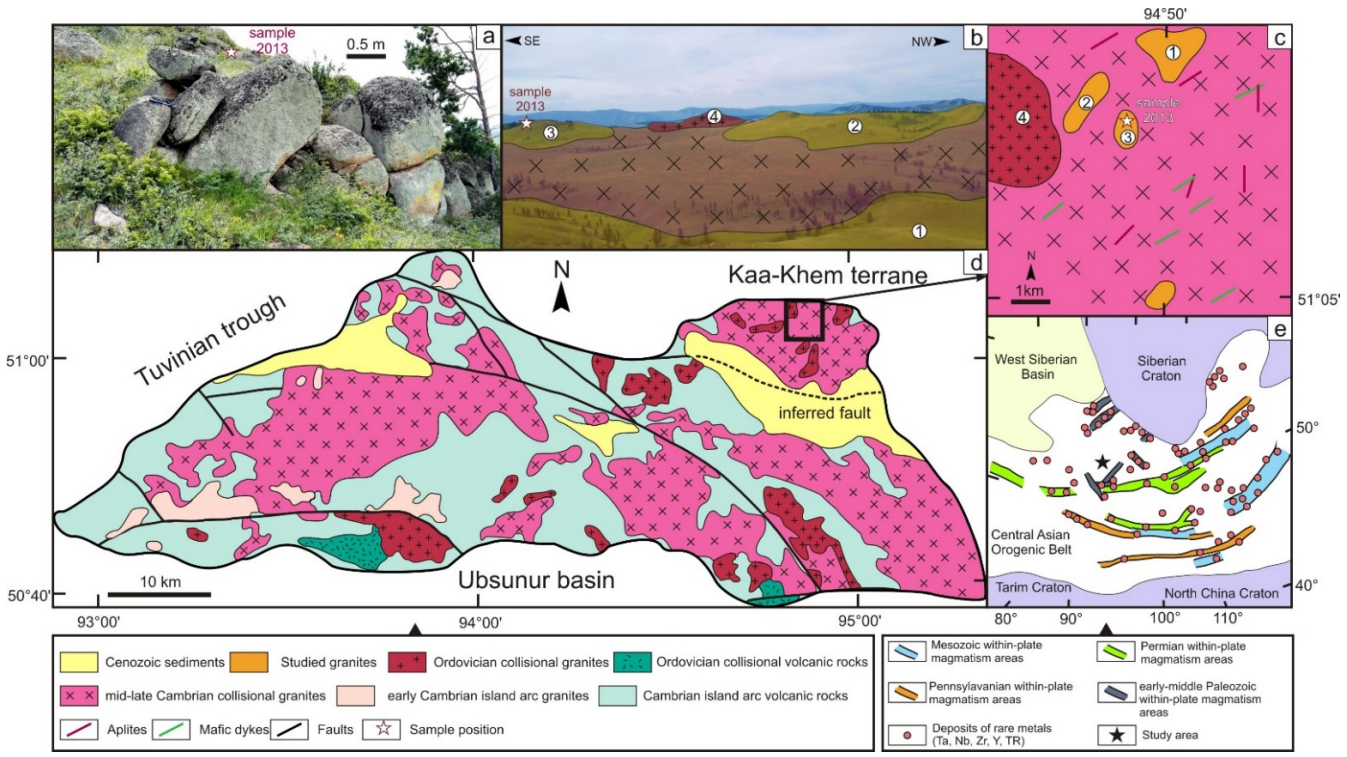

Figure 1. (**a**,**b**) Field photographs of the peralkaline granitic massifs within the Tannuola terrane; (**c**) Simplified geological map showing the study area and sample location; (**d**) Simplified geological map of the Tannuola terrane; (**e**) Deposits of rare metals of the Central Asian Orogenic Belt after [17].

2. Geological Setting

The Tannuola terrane is located in the northern Central Asian Orogenic Belt and extends towards the east for a distance of about 90 km, with a width of 30 km (Figure 1d). It is bordered by the early Paleozoic Kaakhem terrane to the northeast, and it is overlain by the NE-elongated middle-late Paleozoic Tuvinian trough to the northwest, and by the Mesozoic–Cenozoic sediments of the Ubsunur basin to the south.

The Tannuola terrane and the Kaakhem terrane were formed during the Cambrian–Ordovician through subduction and collision events in the southwestern part of the Siberian craton (Figure 1e). The Tannuola terrane consists predominantly of Cambrian island-arc volcanic rocks intruded by numerous granitic rocks with ages from the Early Cambrian to the Late Ordovician (Figure 1d) [18–20]. During the final emplacement of the Tannuola terrane, Middle-Late Ordovician granitoid magmatism was accompanied by felsic volcanism along sub-latitudinal faults in its southern part [21]. In the Early Devonian, fault structures were reactivated and responsible for the evolution of the Tannuola terrane [22], simultaneously with the inception of the Tuvinian trough. The Tuvinian trough is believed to be a NE branch of the triple system of grabens associated with mantle plume activity [23]. The grabens are filled with the Early Devonian thick strata of volcanic rocks, intruded by synchronous mafic dykes, and contain continental terrigenous sediments with ages from the Middle Devonian to the Pennsylvanian [24,25].

For the first time, peralkaline granites were found to occur with the island-arc and collisional granitic rocks of the Tannuola terrane. Previously, in this study area, these types of granites were known only in the neighboring Tuvino-Mongolian microcontinent where the peralkaline granites host rare metal deposits (primarily Ta and Nb) (Figure 2). It is suggested that the peralkaline granites of the Tuvino-Mongolian microcontinent have a Late Pennsylvanian to Early Triassic age of ~300–280 Ma [26,27], and were formed due to the North Asian mantle plume activity [28]. The influence of the Late Pennsylvanian to Early Triassic tectono-magmatic events on the Tannuola terrane is still unclear. However, we recently obtained a zircon U-Pb age of 290 Ma for gabbro from its basement [22], indicating the possible activity of the North Asian mantle plume under the lithosphere of the Tannuola terrane during the Permian.

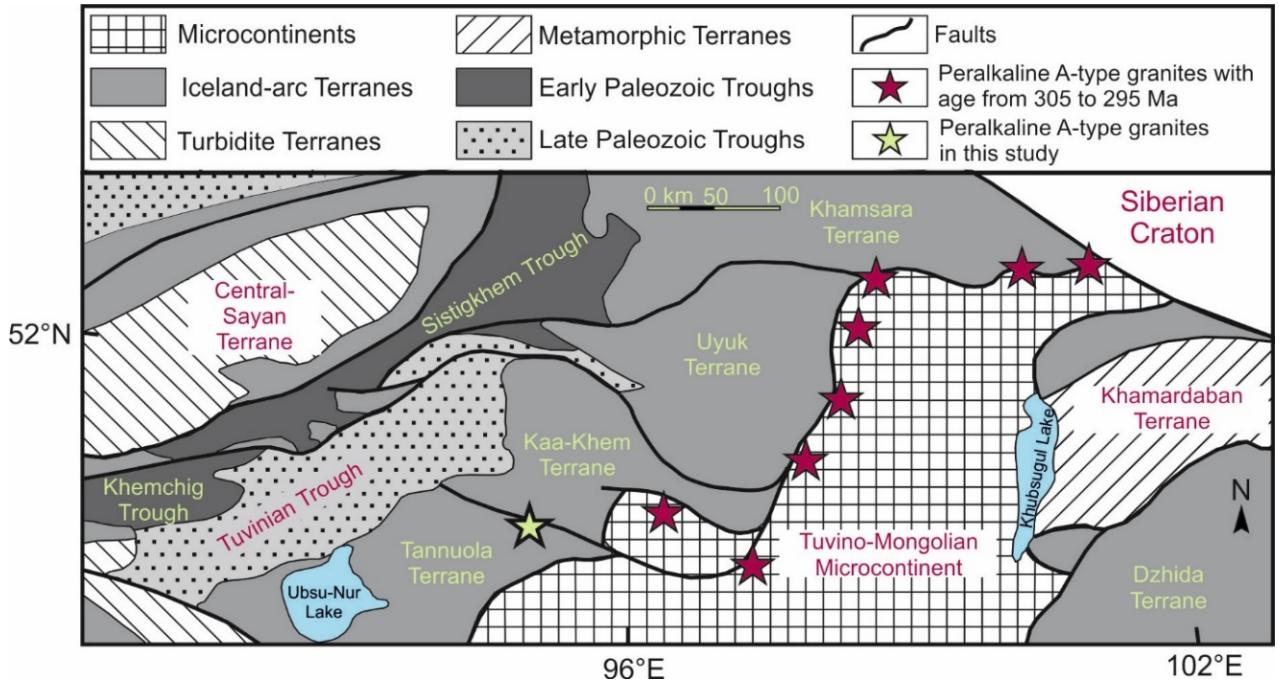

Figure 2. Schematic map showing the position of alkaline magmatism near the Tannuola terrane after [28].

The peralkaline granites of the Tannuola terrane are confined to a sub-latitudinal fault zone. They compose several small scattered massifs of round shape with an area of 0.5–2.5 km^2 (Figure 1a,b) and numerous felsic dykes that intrude the Middle-Late Cambrian granitic rocks (Figure 1c). The granitic massifs include mainly reddish and reddish-gray medium- to coarse-grained riebeckite granites (Figures 3a and 4a), while the felsic dykes comprise gray and brownish fine-grained porphyric aplites (Figures 3b and 4b), with microcline and quartz phenocrysts that are enclosed in a groundmass composed of microcline, plagioclase, quartz, and subordinate riebeckite. Accessory minerals of the peralkaline granites are mainly zircon, apatite, and magnetite. Among the Middle–Late Cambrian granitic rocks, doleritic augite-rich dykes are also common. Some doleritic dykes are intruded by aplites, while others crosscut aplitic dykes. However, enclaves, mingling structures, and other signs of magma mixing are indistinct. Most likely, they were emplaced about the same time, along with aplitic dykes, during several episodes of magmatic impulses. Dolerites are gray-colored fine- to medium-grained rocks with sub-ophitic and poikilitic textures characterized by leucocratic gray-colored to greenish crystals (Figure 3c). They contain euhedral to subhedral plagioclase (55%–60% vol.), clinopyroxene (35%–40%), and orthopyroxene (up to 5%) (Figure 4c). Iron oxides (titano-magnetite), apatite, epidote, chlorite, and carbonate are minor phases. Doleritic dykes include plagioclase phenocrysts (up to 1 mm) and fine-grained Ti-augite.

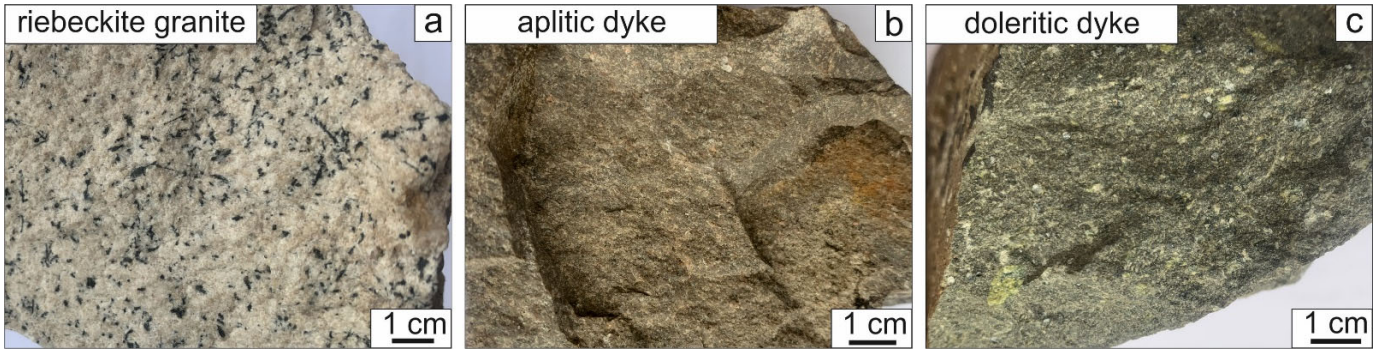

Figure 3. Photographs of (**a**) riebeckite granite sample, (**b**) aplitic dyke sample, and (**c**) doleritic dyke sample from the Tannuola terrane.

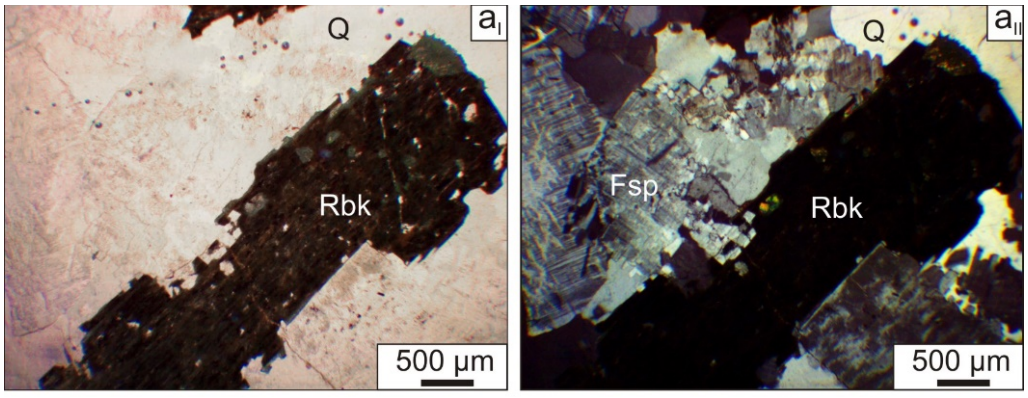

Figure 4. *Cont.*

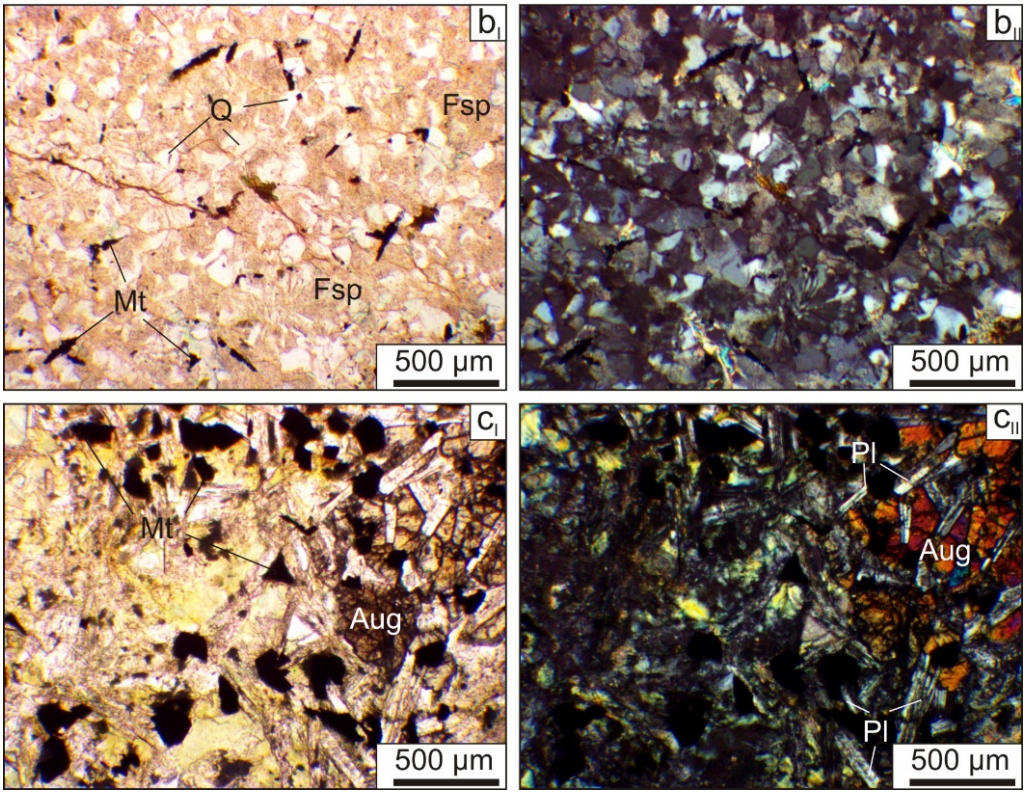

Figure 4. Microphotos of ($\mathbf{a}_{\mathrm{I}}$) riebeckite granite in plane-polarized light, ($\mathbf{a}_{\mathrm{II}}$) riebeckite granite in cross-polarized light, ($\mathbf{b}_{\mathrm{I}}$) aplitic rock in plane-polarized light; ($\mathbf{b}_{\mathrm{II}}$) aplitic rock in cross-polarized light; ($\mathbf{c}_{\mathrm{I}}$) doleritic rock in plane-polarized light, and ($\mathbf{c}_{\mathrm{II}}$) doleritic rock in cross-polarized light from the Tannuola terrane. Pl—plagioclase; Fsp—K-feldspar; Q—quartz; Rbk—riebeckite; Aug—augite; Mt—magnetite.

3. Analytical Methods

We applied in-situ zircon U-Pb dating of the granitic rocks in order to determine the age of the magmatism, and geochemical analyses, including Rb-Sr and Sm-Nd isotope composition of the whole rock samples, with the aim of better understanding their origin and magma sources. Fresh samples were taken from granitic massifs, and doleritic and aplitic dykes.

3.1. Zircon U-Pb Geochronology

A sample (2013, N 51°07′15″, E 94°49′24″) of the granite from one of the massifs (massif №3 in Figure 1b,c) was used for zircon separation and U-Pb dating in this study. Zircon grains were separated through crushing, panning, conventional heavy liquid, and magnetic separation techniques, followed by handpicking under a binocular microscope. The representative zircon grains were mounted in epoxy and polished to half of their thickness. Cathode luminescence (CL) and backscattered electron imaging were used to examine the size, morphology, and internal structure of the zircon grains, and to avoid defective grains with mineral inclusions and micro-fractures. CL imaging was performed using a Scanning Electron Microscope JEOL JSM-6400 SEM at the A. P. Karpinsky Russian Geological Research Institute (St. Petersburg, Russia). The analytical measurements were performed according to the standard method [29] using a sensitive high-resolution ion-microprobe (SHRIMP-II) technique at the Center of Isotopic Research, A. P. Karpinsky Russian Geological Research Institute (St. Petersburg, Russia). The diameter of the spot was about 18 μm, and the primary beam intensity was about 4 nA. Zircon TEMORA with an age of 416.75 Ma [30] was used as an age calibration standard. Corrections for common Pb were made using measured ^{204}Pb isotope and by applying the Pb-isotopic composition

of Stacey and Kramers [31]. Uncertainties about individual analyses and calculated ages are reported at the 2 σ level in Table 1. The age calculations, Concordia (Wetherill) plot, single-grain, and weighted mean $^{206}Pb/^{238}U$ dates were obtained using IsoplotR software (version 5.0, London Geochronology Center, London, UK) [32].

3.2. Whole-Rock Major and Trace Elements Analyses

Thirteen representative samples from granitic massifs, six aplite samples, and five samples from mafic dykes were first crushed and subsequently pulverized. Analysis of major element compositions was performed at the Siberian Research Institute of Geology, Geophysics and Mineral Resources (Novosibirsk, Russia) using X-ray fluorescence (XRF) techniques. The accuracies of the XRF analyses for the major element vary from 2% to 5%. Trace elements were analyzed using an ELAN-DRC-6100 ICP mass spectrometer at the Russian Geological Research Institute (St. Petersburg, Russia), following the procedures outlined by Jenner et al. [33]. Analytical precision for trace elements was higher than ±5% for most trace elements. Results of these analyses (in wt % and ppm, respectively) are presented in Table 2.

3.3. Whole-Rock Sr-Nd Isotope Analyses

Whole rock Sr and Nd isotopic compositions of the study granites were determined using a Triton T1 seven-channel solid-state mass spectrometer at the A. P. Karpinsky Russian Geological Research Institute (St. Petersburg, Russia). Details of the analytical procedures for Sr and Nd isotopes may be found in Bogomolov et al. [34]. The accuracy of Sr and Nd isotopic analyses was controlled by analysis of the VNIIM-Sr ($^{87}Sr/^{86}Sr$ = 0.70801 ± 20) and JNd-1 ($^{143}Nd/^{144}Nd$ = 0.5121003 ± 104) standards, respectively. The reported $^{87}Rb/^{86}Sr$ and $^{147}Sm/^{144}Nd$ values were calculated from the contents of Rb, Sr, Sm, and Nd determined by ICP MS. The εNd(t) and $^{87}Sr/^{86}Sr(T)$ values were calculated with $^{143}Nd/^{144}Nd$ = 0.512638, $^{147}Sm/^{144}Nd$ = 0.1967, 87Rb/86Sr = 0.7045, and $^{87}Sr/^{86}Sr$ = 0.0816 [35]. Two-stage depleted mantle Nd model ages (T_{Nd}) were estimated based on parameters $^{143}Nd/^{144}Nd_{DM}$ = 0.513079, $^{147}Sm/^{144}Nd_{DM}$ = 0.21194, $^{147}Sm/^{144}Nd_{CHUR}$ = 0.1967, $^{143}Nd/^{144}Nd_{CHUR}$ = 0.512638, and $^{147}Sm/^{144}Nd_{CC}$ = 0.13235 [36].

4. Results and Interpretation

4.1. Zircon U-Pb Geochronology

The results of individual SHRIMP zircon U-Pb analyses are given in Table 1. Pb_c and Pb* indicate the common and radiogenic portions, respectively; common Pb was corrected using measured ^{204}Pb; $^{207}Pb/^{235}U$ was calculated using $^{207}Pb/^{206}Pb/(^{238}U/^{206}$ Pb*1/137.88); U and Pb content, and the Th/U ratio, were calculated relative to the reference zircon, the error in Standard calibration was 0.57% and not included in the above errors. Representative zircon CL images, a Concordia diagram, and the weighted mean $^{206}Pb/^{238}U$ age plot, are displayed in Figure 5. Eight zircon grains were analyzed from riebeckite granite (sample 2013). The zircon grains are generally pale yellow and transparent subhedral to euhedral crystals without significant cracks and inclusions. The crystal lengths vary from 120 to 260 μm and the average elongation index ranges from 1.2 to 2.2. CL images demonstrate that most of the zircon crystals contain oscillatory zoning, typical of magmatic origin. Some zircons exhibit different degrees of convolute zoning as the imprint of any post-magmatic event in zircon crystals. Eight spot analyses were performed on areas of zircon crystals with magmatic oscillatory zoning, and a concordant age of 387.7 ± 3.3 Ma was obtained with a concordance probability of 0.93. A weighted mean $^{206}Pb/^{238}U$ value reveals a similar Middle Devonian age of 388.1 ± 3.3 Ma (MSWD = 3.21). The U content varying from 414 to 1024 ppm, Th concentrations ranging from 88 to 684 ppm, and Th/U ratios of the zircons ranging between 0.29 and 0.76, all indicate a magmatic origin for these zircons [37]. All these enable interpretation of the obtained zircon U-Pb age as the magma crystallization age of the studied granitic rocks.

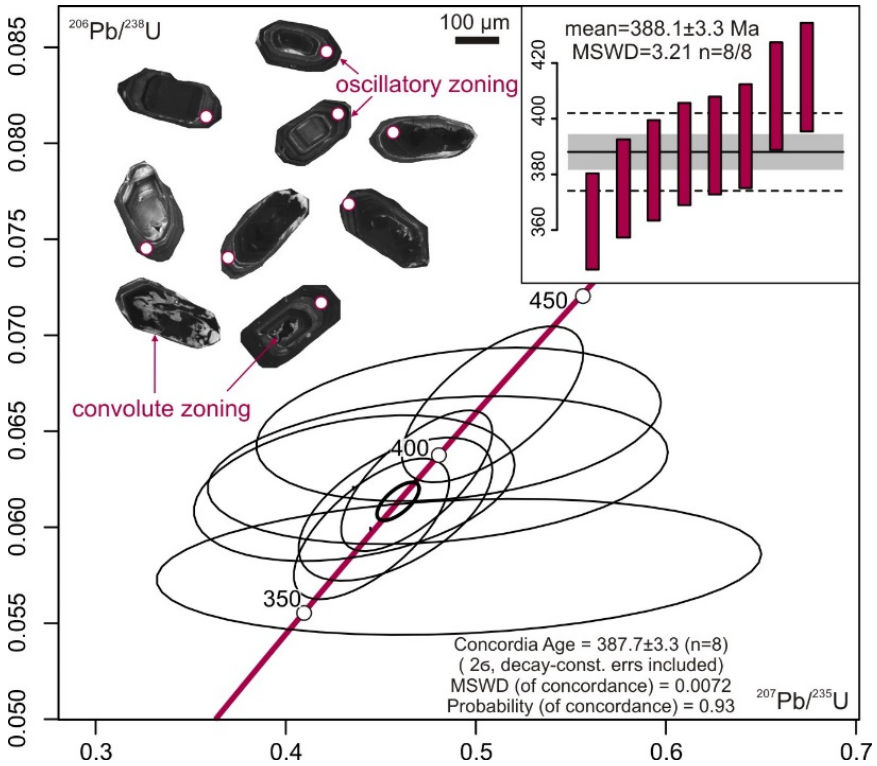

Figure 5. U-Pb isotope Concordia (Wetherill) plot, single-grain, and weighted mean $^{206}Pb/^{238}U$ ages for zircons from the sample of granite (2013). Internal structure of the zircon grains is in cathodoluminescence images. MSWD is given for concordance.

Table 1. U-Pb results (all errors are 2σ).

Spot	$^{206}Pb_{c}$,%	U, ppm	Th, ppm	$^{232}Th/^{238}U$	$^{206}Pb^{*}$. ppm	$^{206}Pb/^{238}U$ Age, Ma		$^{238}U/^{206}Pb^{*}$	±. %	$^{207}Pb^{*}/^{206}Pb^{*}$	±. %	$^{207}Pb^{*}/^{235}U$	±. %	$^{206}Pb^{*}/^{238}U$	± %
13.1	10.77	619	306	0.51	34.5	363	±9	17.26	2.5	0.0615	13.0	0.491	13.0	0.0579	2.5
14.1	0.54	1024	375	0.38	53.0	375	±9	16.69	2.5	0.0539	2.8	0.445	3.7	0.0599	2.5
15.1	0.78	307	88	0.30	16.2	381	±9	16.41	2.5	0.0545	3.8	0.458	4.6	0.0609	2.5
16.1	8.11	781	590	0.78	45.3	388	±9	16.12	2.5	0.0510	7.5	0.436	7.9	0.0620	2.5
17.1	0.63	1021	684	0.69	55.1	390	±9	16.02	2.4	0.0545	2.5	0.469	3.5	0.0624	2.4
18.1	0.99	414	171	0.43	22.6	394	±10	15.88	2.5	0.0553	10.0	0.481	11.0	0.0630	2.5
19.1	5.15	576	322	0.58	34.1	408	±10	15.30	2.5	0.0545	8.5	0.491	8.8	0.0654	2.5
20.1	1.05	584	345	0.61	33.7	414	±10	15.06	2.5	0.0556	2.9	0.509	3.8	0.0664	2.5

4.2. Whole-Rock Major and Trace Elements Geochemistry

4.2.1. Granitic Rocks

The whole-rock geochemical data for the thirteen granites and six aplites are listed in Table 2. Generally, the granites from massifs and aplites from dykes have similar geochemical compositions, consistent with the pattern of A-type granites [38,39]. They have an extremely high content of SiO_2 (75.2−78.2 wt %) and a variable alkali ($Na_2O + K_2O$) content, from 6.0 wt % to 8.9 wt % (Figure 6a). These granitic rocks are characterized by a low content of major rock-forming elements: Al_2O_3 (10.3–12.2 wt %), MgO (0.10–0.51 wt %), CaO (0.07–0.85 wt %), TiO_2 (0.01–0.17 wt %), and P_2O_5 (0.03–0.05 wt %); $Fe_2O_{3\ total}$ varies from 1.2 to 4.0%. Based on the classification proposed by Frost et al. [40], both granites and aplites are peralkaline (A/CNK = 0.83–1.30 and A/NK = 0.85–1.36, Figure 6b), ferroan ($Fe_2O_{3\ total}/(MgO + Fe_2O_{3\ total})$ = 0.80–0.98, Figure 6c), and calc-alkalic to alkali-calcic ($Na_2O + K_2O$-CaO = 5.8–8.5 wt %, Figure 6d).

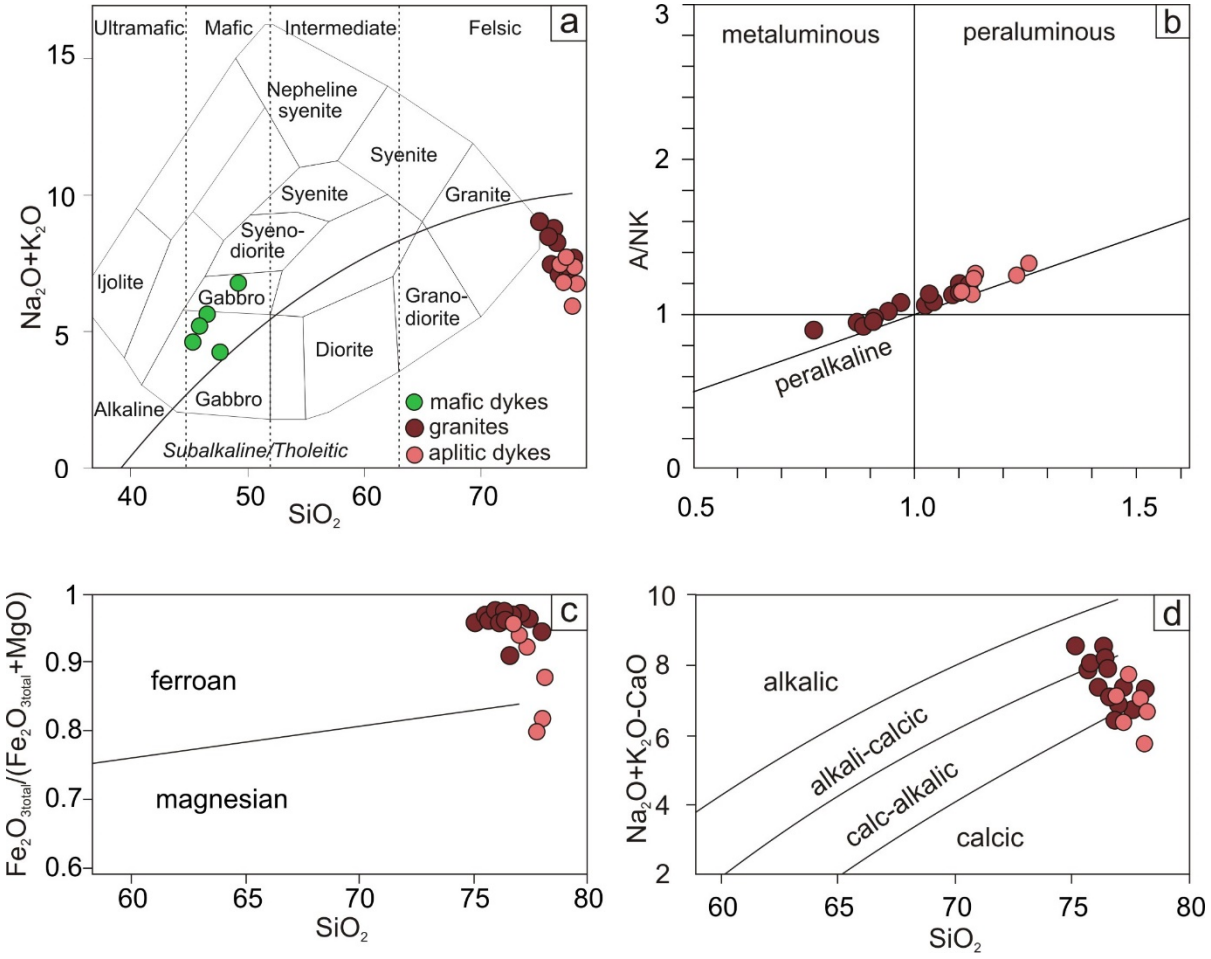

Figure 6. (**a**) TAS diagram (fields according to [41]); (**b**) $Al_2O_3/(CaO + Na_2O + K_2O)$–$Al_2O_3/(Na_2O + K_2O)$ diagram (molecular amounts) [42]; (**c**) SiO_2–$Fe_2O_{3total}/(Fe_2O_{3total} + MgO)$ diagram [40]; and (**d**) SiO_2–MALI diagram [40].

The granites and aplites have a high total content of rare earth elements (ΣREE = 153–678 ppm). They reveal the highly fractionated chondrite-normalized REE patterns (Figure 7a) with enrichment of high REE ($(La/Yb)_N$ = 0.68–7.68) and strong negative Eu anomalies (Eu/Eu* = 0.09–0.23). On the primitive mantle-normalized trace element diagrams (Figure 7c), all samples show strong enrichment in Ta (4.46–36.70 ppm), Pb (2.52–51.00 ppm,) and Zr (417–2530 ppm), and depletion of Ba (9.7–193.0 ppm), Sr (3.14–44.20 ppm), and Ti (60–1020 ppm). Zirconium content of the granites and aplites, ranging from 417 to 2530 ppm, yields high zircon saturation temperatures of 923−1184 °C, with an average of 1030 °C according to the Watson and Harrison [43] equation. On the tectonic discrimination diagrams (Figure 8), all the analyzed samples fall in the within-plate granite field, indicating that studied granitic rocks were formed in an intraplate setting.

Table 2. Major (in wt %) and trace elements (in ppm) data for the peralkaline granitic and coeval mafic rocks from the Tannuola terrane.

Sample	Granites												
	2013	**2010-1**	**2010**	**2054-1**	**106-3**	**2012-2**	**2012-1**	**106-1**	**2012**	**2054-2**	**2054**	**106-6**	**106-5**
SiO_2	75.2	75.7	75.8	76.1	76.3	76.4	76.5	76.7	76.8	76.9	77.1	77.5	78.1
TiO_2	0.13	0.13	0.12	0.15	0.08	0.10	0.04	0.12	0.17	0.14	0.14	0.14	0.08
Al_2O_3	11.4	10.6	11.5	10.6	11.2	10.3	11.5	10.9	10.3	10.6	10.6	10.8	11.4
Fe_2O_{3total}	2.55	3.40	3.14	4.52	2.61	3.99	2.66	3.72	3.42	4.21	3.96	3.05	1.82
MnO	0.05	0.01	0.07	0.01	0.01	0.07	0.06	0.01	0.08	0.01	0.03	0.01	0.02
MgO	0.10	0.10	0.10	0.10	0.10	0.10	0.10	0.36	0.10	0.14	0.10	0.10	0.10
CaO	0.42	0.29	0.36	0.07	0.16	0.10	0.27	0.15	0.85	0.11	0.05	0.48	0.40
Na_2O	4.6	4.0	4.2	3.6	4.5	4.4	5.7	3.6	6.9	3.5	3.8	4.4	3.5
K_2O	4.4	4.2	4.3	3.8	4.3	3.9	2.6	3.5	0.4	3.5	3.7	2.8	4.2
P_2O_5	0.05	0.05	0.05	0.05	0.05	0.04	0.05	0.05	0.01	0.06	0.02	0.05	0.05
LOI	0.79	0.82	0.44	0.43	0.33	0.26	0.29	0.66	0.68	0.57	0.45	0.67	0.55
Total	99.47	99.17	99.94	99.41	99.50	99.49	99.69	99.70	99.60	99.75	99.81	99.98	100.00
Sc	5.25	3.26	3.59	24.10	3.47	2.03	3.34	3.93	2.54	23.70	16.60	4.35	2.51
Co	0.72	0.52	0.68	1.28	0.51	0.50	0.57	2.59	2.06	1.40	1.21	0.82	0.68
Ni	3.12	3.79	4.08	7.42	1.56	1.87	2.88	2.68	2.80	4.32	4.28	5.00	3.77
Cu	3.79	4.55	4.94	8.81	3.02	4.90	2.92	116.00	6.73	6.37	8.08	8.63	11.60
Pb	51.00	47.70	33.00	11.60	47.90	25.30	17.30	26.40	33.40	13.10	13.90	22.60	8.95
V	2.50	2.50	2.50	4.52	2.50	2.50	3.21	5.84	8.94	2.50	6.08	2.50	2.50
Cr	26.80	100.00	35.00	136.00	43.80	23.30	81.40	26.90	76.30	98.00	42.80	175.00	30.30
Rb	140.0	154.0	141.0	167.0	152.0	177.0	132.0	235.0	13.9	162.0	151.0	107.0	146.0
Sr	20.10	17.60	12.50	11.80	6.63	3.14	5.29	13.00	44.20	10.10	9.27	16.60	8.36
Y	127.0	107.0	102.0	391.0	56.1	42.9	124.0	157.0	298.0	319.0	245.0	137.0	46.8
Zr	636	608	904	2530	904	417	591	1350	1620	2510	1410	1250	666
Nb	107.0	96.8	79.7	300.0	105.0	55.8	64.7	196.0	374.0	294.0	231.0	216.0	69.7
Cs	0.65	0.78	1.08	0.53	0.85	1.02	0.84	1.17	0.10	0.44	0.45	0.73	1.25
Ba	59.2	14.5	20.8	161.0	16.4	9.7	11.2	48.3	30.5	161.0	106.0	35.8	26.3
La	47.4	44.0	56.8	83.5	46.1	24.0	71.6	21.7	111.0	28.8	48.0	49.0	20.3
Ce	102.0	96.6	126.0	206.0	103.0	69.2	170.0	103.0	230.0	116.0	129.0	167.0	67.0
Pr	12.2	12.8	14.5	23.4	12.4	6.5	18.9	7.0	30.1	10.4	14.4	12.3	5.7
Nd	42.7	48.1	55.0	85.9	46.1	23.1	68.6	26.7	115.0	44.0	52.5	41.5	22.6
Sm	11.30	12.80	13.60	25.50	10.30	5.40	19.20	9.97	28.20	16.00	16.80	10.10	5.52
Eu	0.64	0.60	0.71	1.40	0.42	0.26	0.46	0.46	1.51	0.83	0.95	0.56	0.20
Gd	13.50	12.60	12.40	31.00	8.96	5.51	18.10	13.20	31.70	21.70	19.60	11.10	4.98
Tb	2.46	2.25	2.13	6.66	1.44	1.04	2.90	2.92	5.99	5.40	4.21	2.35	0.97

Table 2. *Cont.*

Sample	Granites												
	2013	**2010-1**	**2010**	**2054-1**	**106-3**	**2012-2**	**2012-1**	**106-1**	**2012**	**2054-2**	**2054**	**106-6**	**106-5**
Dy	17.20	15.80	16.50	57.10	9.75	7.17	21.60	24.30	43.10	48.60	33.80	21.40	7.57
Ho	4.10	3.41	3.42	12.60	2.14	1.68	4.19	5.51	9.47	11.50	8.56	5.37	1.57
Er	12.50	10.40	11.10	42.90	7.01	5.78	12.50	18.70	28.30	39.30	29.20	20.80	5.82
Tm	2.22	1.79	2.00	7.34	1.53	1.06	2.12	3.31	5.23	6.92	4.75	4.44	1.02
Yb	12.80	11.00	14.90	46.60	11.80	7.15	13.00	21.70	33.90	44.00	28.30	28.10	8.15
Lu	1.90	1.65	2.04	6.56	1.75	1.23	1.85	3.24	4.73	6.00	4.02	3.86	1.26
Hf	21.60	18.70	25.10	69.70	25.80	12.80	17.90	38.40	47.00	71.90	52.30	34.30	18.30
Ta	9.08	7.31	7.49	35.80	9.98	4.46	5.62	20.10	36.70	34.70	19.20	25.80	6.65
Th	22.6	15.1	22.6	63.3	23.3	12.1	16.9	30.9	54.6	59.8	44.4	55.6	14.6
U	5.94	4.59	5.37	20.50	5.92	2.52	4.85	10.50	12.30	25.10	12.60	7.89	3.35
ΣREE	283	274	331	636	263	159	425	262	678	399	394	378	153
Eu/Eu*	0.16	0.14	0.16	0.15	0.13	0.14	0.07	0.12	0.15	0.14	0.16	0.16	0.11
Mg#	-	-	2.7	1.9	3.3	-	3.2	8.3	-	2.8	-	2.8	4.7
T_{Zr}· °C	969	967	1021	1180	1018	923	965	1088	1080	1184	1091	1068	991

Sample	Dykes										
	Doleritic Rocks				Aplitic Rocks						
	2019	**114-2**	**2044-1**	**2044-7**	**111-7**	**2044-5**	**2044-3**	**2044-6**	**2044-2**	**1160-6**	**2045**
SiO_2	45.3	45.8	46.4	47.9	49.1	76.9	77.1	77.4	77.9	78.1	78.2
TiO_2	2.61	3.32	2.24	2.31	2.96	0.04	0.06	0.05	0.07	0.05	0.06
Al_2O_3	16.9	14.8	16.7	16.3	16.8	11.7	11.8	12.2	12.1	11.8	11.9
Fe_2O_{3total}	10.91	13.10	9.43	11.70	10.90	2.37	2.39	1.75	1.24	2.34	1.64
MnO	0.19	0.24	0.15	0.16	0.18	0.03	0.01	0.01	0.01	0.01	0.01
MgO	4.59	5.30	5.23	5.65	4.08	0.10	0.15	0.14	0.31	0.51	0.22
CaO	9.87	8.26	9.59	9.08	6.15	0.36	0.52	0.06	0.35	0.26	0.10
Na_2O	3.8	3.6	3.6	3.0	3.9	3.1	3.5	4.0	3.6	4.3	3.8
K_2O	0.7	1.6	2.1	1.1	2.9	4.5	3.4	3.8	3.8	1.7	3.0
P_2O_5	0.72	0.97	0.50	0.51	0.74	0.05	0.06	0.05	0.07	0.05	0.05
LOI	3.81	2.86	3.89	2.18	2.27	0.66	1.13	0.50	0.66	1.03	0.84
Total	99.93	99.89	99.75	99.87	99.95	99.75	100.11	99.90	100.16	100.12	99.74
Sc	24.70	30.20	22.70	22.60	18.90	7.35	7.42	4.18	3.45	7.03	3.73
Co	34.00	36.90	32.70	40.80	27.10	1.34	0.80	0.83	1.01	2.67	1.05
Ni	43.50	31.90	61.50	108.00	13.40	5.13	4.60	3.73	3.48	6.59	4.45

Table 2. *Cont.*

Sample	Dykes										
	Doleritic Rocks					Aplitic Rocks					
	2019	**114-2**	**2044-1**	**2044-7**	**111-7**	**2044-5**	**2044-3**	**2044-6**	**2044-2**	**1160-6**	**2045**
Cu	62.30	47.40	63.30	74.40	21.70	3.68	4.86	7.07	4.29	5.25	3.08
Pb	10.20	9.24	6.61	14.90	8.16	10.20	25.90	9.28	6.35	2.52	19.00
V	273.00	286.00	199.00	233.00	181.00	2.50	2.50	7.16	2.89	2.50	3.59
Cr	101.0	72.8	115.0	123.0	17.8	164.0	106.0	82.5	63.3	152.0	66.4
Rb	7.5	22.0	27.3	9.1	19.2	143.0	84.3	108.0	94.2	40.5	66.4
Sr	816.0	454.0	637.0	542.0	878.0	9.0	15.6	9.8	21.3	34.6	9.2
Y	30.6	36.6	22.8	25.9	28.1	227.0	170.0	179.0	187.0	134.0	105.0
Zr	180.0	218.0	172.0	122.0	247.0	840.0	675.0	639.0	752.0	609.0	672.0
Nb	21.0	20.4	26.6	20.4	37.3	62.9	63.2	67.3	67.9	72.0	72.8
Cs	0.10	0.22	0.20	0.38	0.15	0.47	0.29	0.49	0.42	0.46	0.37
Ba	152	610	294	226	654	65	101	112	136	130	193
La	19.90	26.40	24.00	17.40	33.30	31.90	25.20	29.00	32.20	19.60	8.54
Ce	45.7	61.4	50.3	37.2	67.4	87.2	75.5	86.4	91.3	52.1	47.2
Pr	6.02	7.76	6.13	4.63	7.80	12.40	10.20	12.10	12.40	7.25	4.60
Nd	25.4	36.6	26.3	22.5	33.5	56.8	45.4	53.1	52.1	34.6	21.3
Sm	6.34	8.10	5.52	5.62	7.05	20.80	16.70	17.90	16.00	10.70	9.52
Eu	2.02	2.44	2.04	2.02	2.10	0.95	0.81	0.54	0.75	0.86	0.48
Gd	6.13	7.59	5.60	5.67	6.39	23.10	19.20	20.50	18.40	12.00	10.60
Tb	0.88	1.10	0.73	0.79	0.86	4.28	3.66	3.85	3.81	2.58	2.42
Dy	5.58	7.16	4.44	4.69	5.25	33.20	27.30	30.10	30.10	21.60	20.20
Ho	1.19	1.40	0.88	0.92	0.97	7.14	6.07	6.85	6.50	5.22	4.59
Er	3.26	3.76	2.13	2.61	2.81	22.30	19.10	21.20	20.70	18.40	14.70
Tm	0.41	0.52	0.34	0.38	0.43	3.65	3.26	3.42	3.43	3.39	2.52
Yb	2.52	3.27	1.85	2.22	2.65	22.20	21.80	23.80	21.30	20.60	17.50
Lu	0.41	0.47	0.30	0.31	0.36	3.11	3.06	3.20	3.07	2.94	2.53
Hf	4.30	4.55	3.50	2.61	5.05	28.00	22.90	22.70	26.80	24.30	24.60
Ta	0.33	0.39	0.47	0.36	0.79	6.92	5.89	6.88	6.52	6.92	7.44
Th	1.00	1.39	2.00	1.30	3.22	10.40	16.10	16.10	9.82	15.90	18.10
U	0.47	0.66	0.79	0.45	1.15	4.55	5.12	4.20	4.30	5.67	4.08
ΣREE	126	168	131	107	171	329	277	312	312	212	167
Eu/Eu*	0.98	0.94	1.11	1.08	0.94	0.13	0.14	0.09	0.13	0.23	0.15
Mg#	-	34.7	47.4	41.4	32.1	3.6	5.4	-	-	18.7	-
T_{Zr}. °C	-	-	-	-	-	1025	1000	993	1013	995	1006

Mg# = MgO/(MgO + FeO)·100, in mol; Eu/Eu* = Eu*n*/((Sm*n* + Gd*n*)/2), where Eu*n*, Sm*n*, and Gd*n* are chondrite-normalized concentrations.

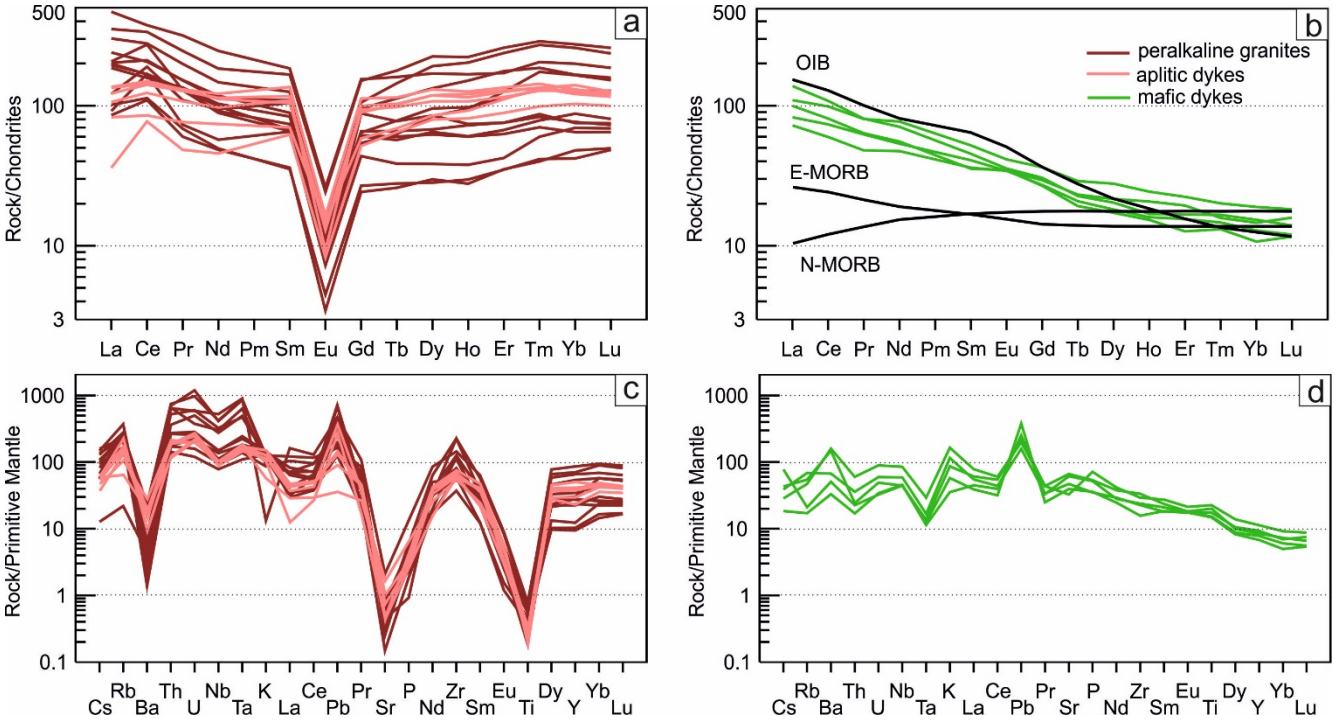

Figure 7. REE (**a**,**c**) and multi-elemental (**b**,**d**) patterns of the peralkaline granitic and coeval mafic rocks of the Tannuola terrane, normalized, respectively, to chondrite [44] and primitive mantle [45].

4.2.2. Mafic Rocks

The samples of doleritic dykes have a low SiO_2 content, ranging from 45.3 to 49.1 wt %, and a high total alkali ($Na_2O + K_2O$) content of 4.1–6.8 wt %, demonstrating alkaline signatures with the composition of gabbro in the TAS diagram (Figure 6a). Dolerites are characterized by high Al_2O_3 (14.8–16.9 wt %), TiO_2 (2.61–3.32 wt %), MgO (4.1–5.7 wt %), P_2O_5 (0.50–0.97 wt %), and moderate compositional variations of $Fe_2O_{3\ total}$ (9.4–11.7 wt %) and CaO (6.2–9.9 wt %). Their Mg# values are low ranging, from 32.1 to 47.4, indicating that they experienced minor to moderate differentiation. The analyzed samples of dolerites contain variable Cr (18–123 ppm) and Ni (13–108 ppm), and a high ΣREE content, ranging from 107 to 171 ppm. In chondrite-normalized REE diagrams (Figure 7b), doleritic rocks are characterized by enrichment in light REE relative to heavy REE with $(La/Yb)_N$ = 11.01–18.09, and an absence of significant Eu anomaly (Eu/Eu* = 0.94–1.11). They show compositional patterns ranging from enriched MORB (E-MORB) to OIB (oceanic-island-basalt). Primitive mantle-normalized trace element diagrams (Figure 7d) show depletion of Ta (0.33–0.79 ppm) and Th (1.00–3.22 ppm) and enrichment in Pb (8.16–14.90 ppm), Sr (454–878 ppm), and Ti (13,440–15,680 ppm).

4.3. Whole-Rock Sr-Nd Isotopes

Whole rock Sr and Nd isotopic data from four representative samples (2010, 2011, 2012–2, 2013) of riebeckite granites, demonstrating homogeneous isotopic composition, are presented in Table 3. Initial Sr-Nd isotopic compositions and εNd(t) values were calculated using the determined zircon U-Pb age of 388 Ma of the riebeckite granite. The calculated initial $^{87}Sr/^{86}Sr$ ratios range from 0.711497 to 0.739895. However, these Sr isotopic values do not reflect any petrogenetic significance due to extremely high $^{87}Rb/^{86}Sr$ values ranging from 28.50 to 112.91, $^{87}Sr/^{86}Sr$ values between 0.867348 and 1.357252, and Rb/Sr > 1, indicating large uncertainties in the calculation of the initial $^{87}Sr/^{86}Sr$ values. Hence, discussion concerning the magma source of granitic rocks can be based on whole-rock Nd isotopic values, as well as major and trace element composition. The initial $^{143}Nd/^{144}Nd$

ratios vary from 0.512445 to 0.512477, with positive εNd(t) values of +5.59 to +6.52. The calculated two-stage model ages for riebeckite granites range from 610 to 520 Ma (Table 3).

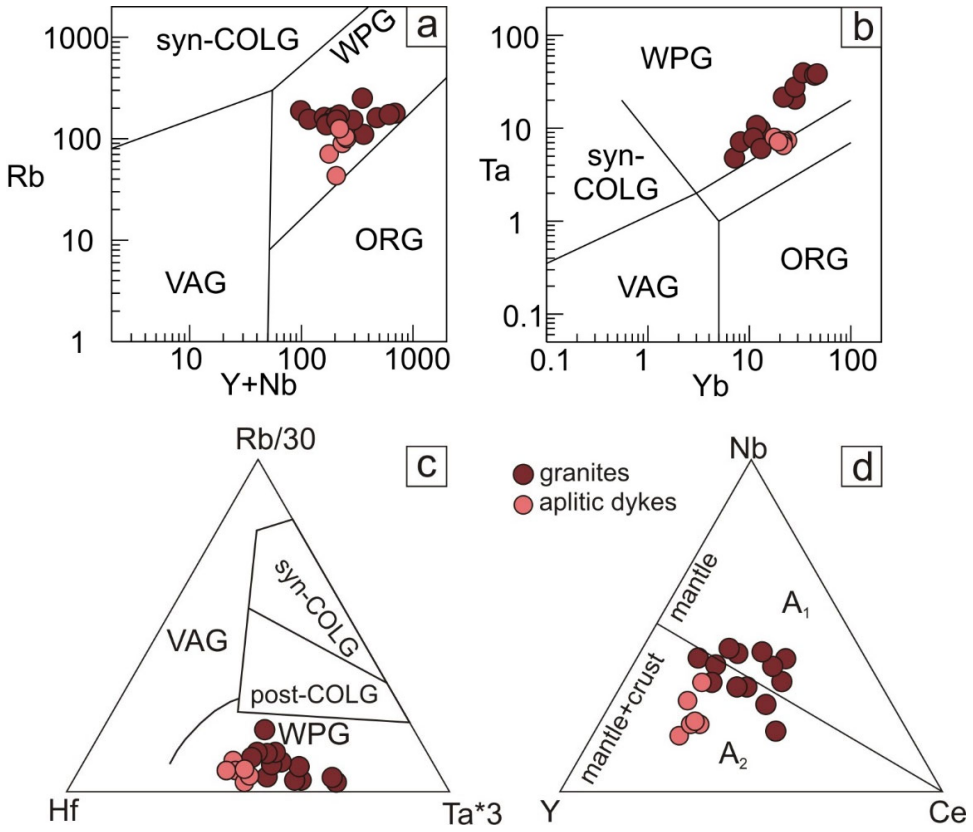

Figure 8. Tectonic diagrams for the peralkaline granitic rocks of the Tannuola terrane. (**a**,**b**) «Y + Nb–Rb» and «Yb–Ta» [46]; (**c**) Rb/30–Hf–Ta·3 ternary diagram [47]. Fields: ORG—ocean ridge granites, VAG—volcanic arc granites, Syn-COLG—syn-collision granites, Post-COLG—post-collision granites, WPG—within plate granites; (**d**) «Y–Nb–Ce» [5].

Table 3. Sr-Nd isotopic compositions for representative samples of the Middle Devonian peralkaline A-type granitic rocks from Tannuola terrane.

Sample	2013	2012-2	2010	2011
Rb (ppm)	134.1	189.5	144.8	151.9
Sr (ppm)	14.0	5.2	13.0	8.0
$^{87}Rb/^{86}Sr$	28.5	112.9	31.9	57.0
±2 σ	0.2850	1.1291	0.3186	0.5702
$^{87}Sr/^{86}Sr$	0.867348	1.357252	0.886572	1.036868
±2 σ	0.000009	0.000009	0.000009	0.000007
$(^{87}Sr/^{86}Sr)_0$	0.867348	1.357252	0.886572	1.036868
Sm (ppm)	9.66	19.35	12.29	2.78
Nd (ppm)	36.06	62.30	43.90	11.31
$^{147}Sm/^{144}Nd$	0.16200	0.15430	0.16910	0.14860
±2 σ	0.00016	0.00015	0.00017	0.00015
$^{143}Nd/^{144}Nd$	0.512860	0.512833	0.512855	0.512851
±2 σ	0.000004	0.000004	0.000005	0.000006
$(^{143}Nd/^{144}Nd)_0$	0.512860	0.512833	0.512855	0.512851
±2σ	0.000027	0.000019	0.000006	0.000010
$\varepsilon_{Nd}(t)$	6.06	5.91	5.61	6.55
$T_{(DM1),}$ Ma	1060	1040	1180	940
$T_{(DM2),}$ Ma	560	580	610	520

5. Discussion

5.1. Geochemical Evidences for A-Type Granitic Rocks and Emplacement Age

Based on geochemical features, granitic rocks are generally divided into I-, S-, or A-types [38,48]. I-type granites are characterized by their metaluminous to slightly peraluminous nature and the presence of hornblende, whereas S-type granites are peraluminous and contain peraluminous minerals, such as muscovite, garnet, cordierite, etc. It is thought that A-type granites comprise alkaline minerals and have a peralkaline nature, high concentrations of SiO_2, K_2O, (K_2O + Na_2O), Zr, Ce, Nb, REE, and a low content of MgO, CaO, Cr, Ni, Ba, Sr, and Eu [38,39]. The riebeckite granites and aplites in this study have a high content of SiO_2 (75.2−78.2 wt %), an alkali (Na_2O + K_2O) content (6.0–8.9 wt %), Zr (417–2530 ppm), and a total content of REE (ΣREE = 153–678 ppm). The A-type granites also contain a low content of CaO (0.07–0.85 wt %), MgO (0.10–0.51 wt %), Ba (9.7–193.0 ppm), Sr (3.14–44.20 ppm), and Eu (0.26–1.51 ppm), with high $Fe_2O_{3\ total}$/(MgO + $Fe_2O_{3\ total}$) ratios (0.80–0.98), indicating the features of A-type granite. They display extremely low Ba, Sr, P, and Ti concentrations on the primitive mantle-normalized trace element diagrams (Figure 7c) and a V-shape in chondrite-normalized REE patterns with distinctly negative Eu anomalies (Figure 7a), suggesting a high degree of fractional crystallization.

The zircon saturation temperature (i.e., initial magma temperatures, T_{Zr}) of granitic rocks range from 923 to 1184 °C, with an average of 1030 °C. Due to inherited zircon grains not being observed, the calculated temperatures provide the minimum estimates [49]. Estimated temperatures are significantly higher than those of S- and I-type granites, which are usually lower than 800 °C [50]. Therefore, granitic rocks in our study can be considered to be A-type granites. According to the geochemical classification by [5], riebeckite granites fall into both the fields of A_1- and A_2-type granites, while the aplites correspond to the highly fractionated A_2-type granites (Figure 8d).

As previously shown, the zircon U-Pb age of 387.7 ± 3.3 Ma for the peralkaline A-type granites from the Tannuola terrane represents the timing of their crystallization and corresponds to the Eifelian–Givetian period boundary. The peralkaline A-type granites with an Eifelian–Givetian age were revealed within the Tannuola terrane for the first time, requiring discussion of their petrogenesis, magma source, and tectonic and geodynamic setting.

5.2. Origin of the Peralkaline A-Type Granites from Tannuola Terrane

The A-type granitic rocks worldwide can be attributed to three main petrogenetic models, including: (1) low degrees of partial melting of crustal rocks [38,39]; (2) hybridization between mantle-derived basaltic and crustal-derived granitic magmas [51,52]; and (3) extensive fractional crystallization of alkaline transitional or tholeitic basaltic magma with crustal contamination [5,53]. Because mafic to intermediate microgranular enclaves and mingling structures could not be found, the peralkaline A-type granitic rocks of the Tannuola terrane were not likely formed through the mixing of the mantle- and crustal-derived magmas. The horizontal trends in the La/Yb versus La diagram (Figure 9a) and the Zr/Nb versus Zr diagram (Figure 9b) reveal the dominant role of fractional crystallization, as opposed to the partial melting process, during the magma evolution of our granitic rocks. These granitic rocks demonstrate a highly fractionated geochemistry and have positive εNd(t) values (+5.59 to +6.52), indicating their formation through fractional crystallization of mafic magma. Moreover, A-type granitic rocks derived through crustal melting show generally peraluminous, rather than peralkaline, composition [54]. Thus, we consider fractional crystallization of mantle-derived magmas in combination with crustal contamination as being the most important mechanism.

Significant depletion of Ba, Sr, P, Ti, and Eu indicates an advanced fractional crystallization during the formation of the riebeckite granites and aplites (Figure 7a,c). Strong depletion of the Eu, Ba, and Sr of the study granitic rocks requires extensive fractionation of plagioclase and/or K-feldspar. K-feldspar crystallization is supported by the K_2O decreasing with increasing SiO_2, while the fractional crystallization of plagioclase can also be inferred from the strong negative anomaly of Eu in the chondrite-normalized REE pattern

(Figure 7a). The depletion of P and Ti might be related to the fractional crystallization of apatite and iron oxides. On the other hand, crustal contamination can lead to depletion of P and Ti. The peralkaline A-type granitic rocks of the Tannuola terrane are enriched in Pb and Zr, and have high ratios of immobile trace elements, such as La/Sm (up to 4.9) and $(Th/Nb)_N$ (>1), typical of crustal rocks [55,56] as well as low Ti/Zr (up to 1.4) and Ti/Y (up to 10.3) ratios [57]. On the $(Th/Yb)_{PM}$–$(Nb/Yb)_{PM}$ diagram (Figure 10a), the aplite samples lie in the field and reflect the composition of the lower continental crust, while the riebeckite granites demonstrate a higher degree of crustal contamination. All these geochemical features of the peralkaline A-type granites from the Tannuola terrane might indicate a significant role of crustal contamination in their petrogenesis, along with fractional crystallization processes.

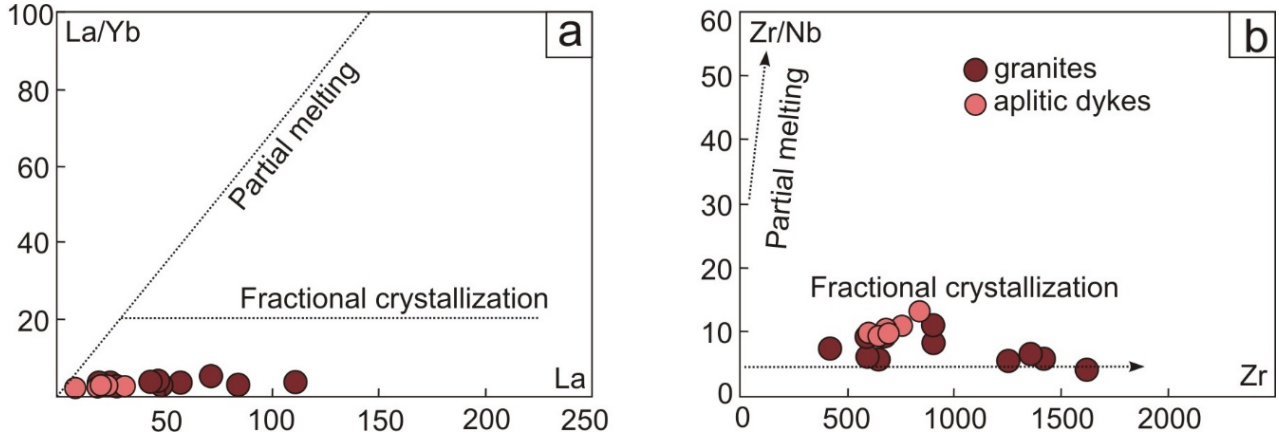

Figure 9. Binary diagrams showing the dominant role of the fractional crystallization process during the evolution of magma for peralkaline granitic rocks from the Tannuola terrane: (**a**) La/Yb–La; (**b**) Zr/Nb–Zr.

5.3. Magma Source

As discussed above, the peralkaline A-type granites from the Tannuola terrane were derived from mantle sources through the fractional crystallization process. This is supported by the diagrams of Laurent et al. [58] despite some samples being shifted in the field of crustal-derived magmas in the $(La)_N$ Fe_2O_3t + MgO plot (Figure 10d,e). Generally, rocks formed by fractionation of mantle-derived magmas have a lower Th/Ta ratio (≈2) compared with the lower crust (Th/Ta ≈ 7.9) and the upper crust (Th/Ta ≈ 6.9) [59,60]. The average Th/Ta values obtained for study granitic rocks are approximately 2 and support the mantle source. Nevertheless, some geochemical characteristics such as their Mg# (up to 19), Cr (up to 175 ppm) and Ni (up to 7 ppm) concentrations are inconsistent with typical mantle-derived magmas (Mg# = 73–81, Cr > 1000 ppm and Ni > 400 ppm) [61]. This could be explained by the high degrees of fractional crystallization from parental magmas and/or the contribution of crustal contamination by magma en route to the surface [62].

Moreover, the peralkaline A-type granitic rocks yield highly positive εNd(t) values, ranging from +5.61 to +6.55 (Table 3). The obtained εNd(t) values are slightly higher those for host Cambrian–Ordovician magmatic rocks of the Tannuola terrane [18–21] and indicate an origin from an enriched mantle source. The calculated Stenian–Tonian one-stage Nd model ages $T_{(DM1)}$ (from 1180 to 940 Ma) are significantly different to those of the Ediacaran–Early Cambrian two-stage Nd model ages $T_{(DM2)}$ (from 610 to 520 Ma). Such large differences between one-stage and two-stage Nd model ages commonly display a high-degree of fractionation and/or heterogeneous sources. As emphasized, the high-degree fractional crystallization played a crucial role in the formation of the study granitic rocks and can explain this discrepancy. The isotopic Sr composition of the peralkaline A-type granites from the Tannuola terrane cannot be used in a discussion about magma

sources due to the extremely high Rb/Sr ratios. The high Rb/Sr ratios most likely relate to fractionation K-feldspar, which could lead to highly variable initial $^{87}Sr/^{86}Sr$ values.

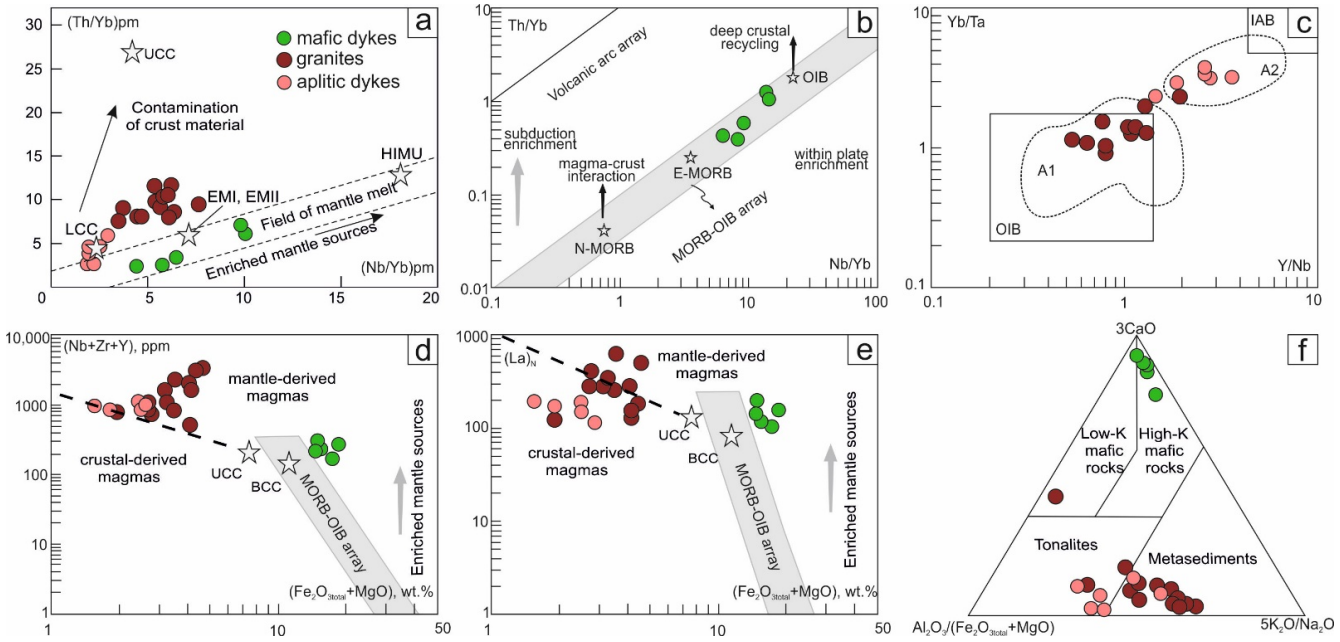

Figure 10. (**a**) (Th/Yb)pm–(Nb/Yb)pm diagram; UCC—upper continental crust; LCC—lower continental crust [63]; EMI, EMII, and HIMU (high μ = $^{238}U/^{204}U$)—enriched mantle [64]; (**b**) Th/Yb–Nb/Yb diagram [65]; (**c**) Yb/Ta-Y/Nb diagram [5]; (**d**) Nb + Zr + Y (ppm) Fe_2O_3t + MgO (wt %) diagram; (**e**) $(La)_N$ Fe_2O_3t + MgO (wt %) diagram [58]; UCC—upper continental crust; BCC—bulk continental crust [60]; MORB—mid-ocean ridge basalts; OIB—ocean island basalts; (**f**) ternary diagram $Al_2O_3/(Fe\ l_2O_3total + MgO)$-3∗CaO-5∗($K_2O/Na_2O$) [58].

According to the Laurent et al. [58] diagram (Figure 10f), the source of peralkaline granitic magma is represented by metasedimentary rocks and/or tonalites, while magma for doleritic dykes originated from the melting of high-K mafic rocks. The metasedimentary source for peralkaline granitic magma can be explained by the enhancing of the partial melting of the crustal rocks by magma en route to the surface. Mafic rocks represent another magma pulse due to the melting of high-K rocks; we, therefore, scrutinized dolerite samples from coeval mafic dykes to better identify the nature of their melt source. Dolerites yield MgO content (4.1–5.7 wt %) and Mg# values (up to 47) lower than those of primitive magmas, indicating the crucial role of fractional crystallization during its magmatic evolution. Fractionation of clinopyroxene (Ti-augite) appears to be more significant in view of the positive correlations of Zr with MgO, Ni, and Cr, and the negative correlations of Zr with MgO, Ni, and Cr. However, the lack of strong negative Eu anomalies (Eu/Eu* = 0.94–1.11) (Figure 7a) and the positive correlations of Zr with P_2O_5, TiO_2, and Sr, suggest that plagioclase and accessory minerals, such as apatite and titano-magnetite, were the minor fractionating phases. Mantle-derived magmas are often subject to crustal contamination during their ascent or storage in a crustal magma chamber [62,66]. Crustal contamination of mafic magmas generally cause the elevation of continental-enriched elements such as Th, Zr, and Hf. The relatively low Th (average = 1.78 ppm), Zr (average = 188 ppm), and Hf (average = 4.00 ppm) concentrations, as well as the enrichment with Nb in the studied dolerite samples, are inconsistent with the effects of significant crustal contamination. In the contamination-sensitive trace element $(Th/Yb)_{pm}$–$(Nb/Yb)_{pm}$ diagram (Figure 10a), the samples lie far from the upper continental crust endmembers, excluding the possibility of crustal contamination and demonstrating a mantle source for the analyzed mafic rocks. Furthermore, the chondrite-normalized REE spectra (Figure 7b) and the Th/Yb-Nb/Yb diagram (Figure 10b) show compositional patterns between E-MORB and OIB. This is con-

sistent with mafic magmas being derived from a geochemically enriched mantle unaffected by subduction-related fluids and/or melts [67]. In turn, the enrichment in incompatible elements with high HFSE/LREE ratios (Nb/La > 1) [68] indicates that the parental magma for analyzed dolerites might have originated from the lithospheric mantle, metasomatized by asthenosphere-derived melt.

5.4. Tectonic Implication

A-type granites are generally emplaced in extensional tectonic regimes: post-collisional or intraplate extensional settings [5,35,69]. A-type granites are subdivided into two subtypes (A_1- and A_2-type granites) based on their trace element composition, especially their Y/Nb ratio and Nb-Y-Ce content, suggesting their different origins. The A_1-type granites have Y/Nb < 1.2 and represent products of fractional crystallization of mantle-derived magmas associated with anorogenic tectonic environments (continental rift or intraplate settings). A_2-type granites with Y/Nb > 1.2, however, are derived from the subcontinental lithosphere or lower crust and emplaced in post-collisional or post-orogenic settings.

The analyzed riebeckite granites have variable Y/Nb ratios (0.53–1.92), with an average value of 1.01, and lie in both the A_1- and A_2-type fields on the Ce–Nb–Y diagram (Figure 8d), while the aplites with high Y/Nb ratios (1.44–3.61), and an average value of 2.50, fall into the A_2-type field without exception. The varying degrees of increase in Y/Nb ratios of peralkaline A-type granitic rocks from the Tannuola terrane could be caused by crustal contamination shifting their samples toward the A_2 type field. Positive correlations between the ratios of Y/Nb and Yb/Ta (Figure 10c) for the analyzed rocks strongly suggest crustal contamination [5], as proposed above. In addition, on the tectonic diagrams of Rb − (Y + Nb), Ta–Yb and Hf-Rb/30-Ta*3 (Figure 10a–c), all granitic samples lie within the intraplate field, which is consistent with an anorogenic tectonic regime. Similarly, coeval mafic rocks with a chemical composition of E-MORB and OIB are also typical of an intraplate extensional setting.

Emplacement of the peralkaline A-type granitic rocks controlled by a sub-latitudinal deep-seated fault zone mark a short period of extension and subsequent rifting within the Tannuola terrane. This fault activation is probably associated with the evolution of the riftogenic Tuvinian trough during the Devonian to the northwest of the study area. However, during the Middle Devonian, there is no evidence of felsic magmatic activity within the Tuvinian trough, where continental carbonate-terrigenous sediments accumulated at that time. Nevertheless, the extension during the Middle Devonian, proposed in this study, triggered the upwelling of small volume of lithospheric mantle metasomatized by asthenosphere-derived mantle sources and the emplacement of mafic rocks within the Tannuola terrane. The peralkaline A-type granites are related to the mafic rocks in the study area; however, they represent another magma pulse.

5.5. Geodynamic Model

In the Tannuola terrane, peralkaline A-type granitic rocks with an age of 388 Ma are distributed sporadically and are small in volume. This is distinctly different from widespread Cambrian island-arc volcanic rocks or Late Cambrian to Late Ordovician collisional and post-collisional mafic and granitic intrusions [18–20]. The occurrence of coeval mafic intrusions in the Tannuola terrane required vast heat sources and may reflect the upwelling of mafic magmas (Figure 11). However, the emplacement mechanism of mafic magmas in the study area during the Eifelian–Givetian is still unclear. Heat sources are usually attributed to one of the following geodynamic models: (1) delamination of the lower lithosphere, (2) slab break-off, or (3) a rising mantle plume. The lithosphere delamination model suggests that gravity instability within the lower crust occurs in a post-collisional setting [70]. This could result in an asthenosphere upwelling accompanied by crustal extension, which would promote heat input for magma generation. Because the collisional events in this area terminated in the Late Ordovician (~450 Ma), lithospheric delamination does not seem to be a fit geodynamic model. Slab break off can also generate thermal

perturbation and cause asthenosphere upwelling in relation to the crustal extension [71]. It is thought that the asthenospheric mantle rises through a narrow lithosphere gap above the sinking slab, forming a narrow linear zone of magmatism [72]. Peralkaline A-type granitic rocks of the Tannuola terrane do not form a linear configuration, so were unlikely to have originated due to slab break-off. A mantle plume model should be considered as the main emplacement mechanism for an asthenosphere upwelling in the study area. Recently, a mantle plume model was proposed to explain the widespread Devonian magmatism of the northern Central Asian Orogenic Belt areas [23,73,74]. Our geochemical study of the mafic rocks coeval to the peralkaline A-type granitic rocks suggest enriched mantle sources that are generally attributed to mantle plume activity [5]. In addition, the peralkaline A-type granitic rocks of the Tannuola terrane exhibit high zircon saturation temperatures (T_{Zr} = 923−1184 °C, with an average of 1030 °C) typical of granites related to the mantle plume. Therefore, a rising mantle plume was responsible for the magma generation of peralkaline A-type granitic and coeval mafic rocks in the Tannuola terrane.

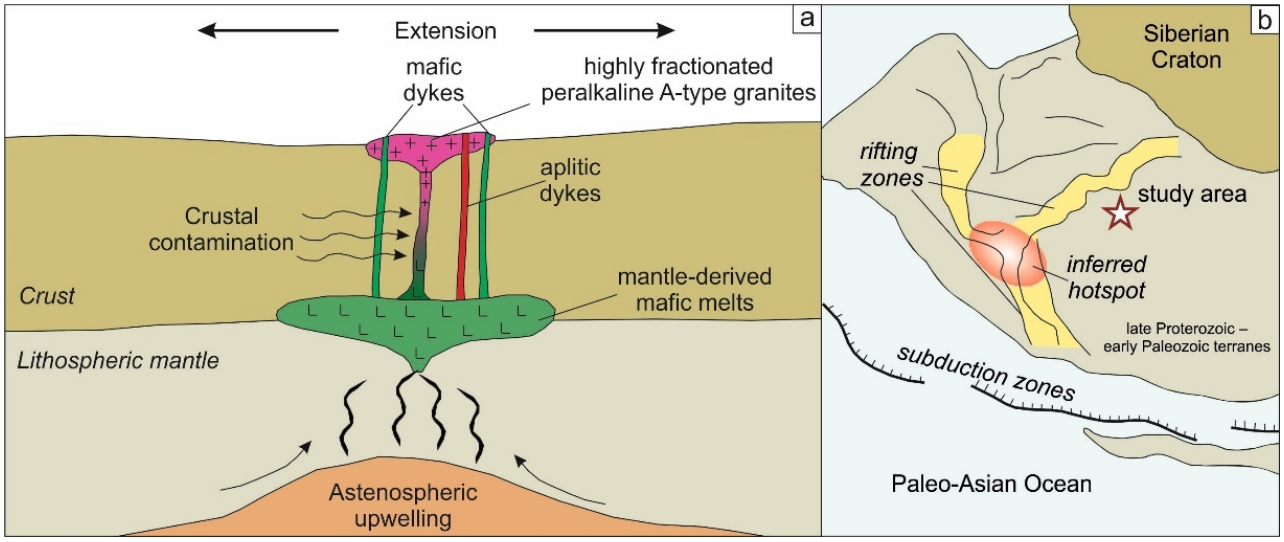

Figure 11. A geodynamic model showing evolution of the peralkaline A-type granitic and coeval mafic rocks of the Tannuola terrane (**a**) within the framework of geodynamic evolution of the northern Central Asian Orogenic Belt and (**b**) during Middle Devonian. Not to scale.

6. Conclusions

Based on the presented results, including zircon SHRIMP U-Pb ages, and geochemical and Sr-Nd isotope compositions, we draw the following conclusions regarding the petrogenesis and tectonic setting of the peralkaline A-type granitic rocks from the Tannuola terrane. Peralkaline A-type granitic rocks were emplaced in the Tannuola terrane at 387.7 ± 3.3 Ma, which corresponds to the Eifelian–Givetian period. Riebeckite granites and aplitic dykes, as well as co-genetic coeval mafic rocks, demonstrate an affinity to a within-plate setting that is consistent with an anorogenic tectonic regime. Geochemical and isotopic compositions suggest that these peralkaline A-type granitic rocks originated from fractional crystallization of enriched mantle sources with crustal contamination. The primary magmas for peralkaline A-type granites originated from juvenile Neoproterozoic–Cambrian (from 610 to 520 Ma) sources with highly positive (from +5.61 to +6.55) εNd(t) values. Asthenospheric upwelling triggered the generation of these magmas. The emplacement of peralkaline A-type granitic rocks marks a short period of extension and rifting within the Tannuola terrane and indicates mantle plume activity beneath the northern Central Asian Orogenic Belt areas during the Givetian period.

Author Contributions: Conceptualization, E.V.V.; formal analysis, E.V.V. and E.A.P.; funding acquisition, E.V.V.; investigation, E.V.V., E.A.P. and N.I.V.; methodology, E.V.V. and E.A.P.; project administration, E.V.V.; resources, E.A.P.; software, N.I.V.; supervision, E.V.V.; visualization, N.I.V.; writing—original draft, E.V.V.; writing—review and editing, N.I.V. All authors have read and agreed to the published version of the manuscript.

Funding: The study was funded by a grant from the Russian Science Foundation (project № 22-77-10069). Evgeny Vetrov was also funded by a grant from the President of the Russian Federation (project MK-3510.2022.1.5.)

Acknowledgments: Three anonymous reviewers are thanked for their constructive comments that greatly improved this article.

Conflicts of Interest: The authors declare no conflict of interest.

References

1. Papp, J.F. Tantalum. Minerals Yearbook 2015. V. I. Metals and Minerals. *U.S. Geol. Surv.* **2018**, *76*, 1–82.
2. Schulz, K.J.; DeYoung, J.H.; Seal, R.R.; Bradley, D.C. (Eds.) Critical mineral resources of the United States—Economic and environmental geology and prospects for future supply. In *U.S. Geological Survey Professional Paper*; United States Government Publishing Office: Washington, DC, USA, 2017; 1802, pp. M1–M34.
3. Bonin, B. A-type granites and related rocks: Evolution of a concept, problems and prospects. *Lithos* **2007**, *97*, 1–29. [CrossRef]
4. Rudnick, R. Making continental crust. *Nature* **1995**, *378*, 571–578. [CrossRef]
5. Eby, G.N. Chemical subdivision of the A-type granitoids:Petrogenetic and tectonic implications. *Geology* **1992**, *20*, 641–644. [CrossRef]
6. Abdel-Karim, A.-A.; Azer, M.; Sami, M. Petrogenesis and tectonic implications of the Maladob ring complex in the South Eastern Desert, Egypt: New insights from mineral chemistry and whole-rock geochemistry. *Geol. Rundsch.* **2020**, *110*, 53–80. [CrossRef]
7. Robinson, F.; Foden, J.; Collins, A. Geochemical and isotopic constraints on island arc, synorogenic, post-orogenic and anorogenic granitoids in the Arabian Shield, Saudi Arabia. *Lithos* **2015**, *220-223*, 97–115. [CrossRef]
8. Papoutsa, A.; Pe-Piper, G.; Piper, D.J. Systematic mineralogical diversity in A-type granitic intrusions: Control of magmatic source and geological processes. *GSA Bull.* **2015**, *128*, 487–501. [CrossRef]
9. Sengör, A.M.C.; Natalin, B.A.; Burtman, V.S. Evolution of the Altaid Tectonic Collage and Paleozoic crustal growth in Eurasia. *Nature* **1993**, *364*, 299–307. [CrossRef]
10. Xiao, W.; Windley, B.F.; Sun, S.; Li, J.; Huang, B.; Han, C.; Yuan, C.; Sun, M.; Chen, H. A Tale of Amalgamation of Three Permo-Triassic Collage Systems in Central Asia: Oroclines, Sutures, and Terminal Accretion. *Annu. Rev. Earth Planet. Sci.* **2015**, *43*, 477–507. [CrossRef]
11. Windley, B.F.; Alexeiev, D.; Xiao, W.; Kröner, A.; Badarch, G. Tectonic models for accretion of the Central Asian Orogenic Belt. *J. Geol. Soc.* **2007**, *164*, 31–47. [CrossRef]
12. Xiao, W.J.; Windley, B.F.; Badararch, G.; Sun, S.; Li, J.; Qin, K.; Wang, Z. Paleozoic accretionary and convergent tectonics of the southern Altaids: Implications for the growth of central Asia. *J. Geol. Soc. Lond.* **2004**, *161*, 1–4. [CrossRef]
13. Jahn, B.M. The Central Asian Orogenic Belt and growth of the contitental crust in the Phanerozoic. In *Aspects of the Tectonic Evolution of China*; Special Publications: London, UK, 2004; Volume 226, pp. 73–100.
14. Dawei, H.; Shiguang, W.; Baofu, H.; Manyuan, J. Post-orogenic alkaline granites from China and comparisons with anorogenic alkaline granites elsewhere. *J. Southeast Asian Earth Sci.* **1996**, *13*, 13–27. [CrossRef]
15. Jahn, B.-M.; Wu, F.; Chen, B. Granitoids of the Central Asian Orogenic Belt and continental growth in the Phanerozoic. *Trans. R. Soc. Edinb. Earth Sci.* **2000**, *91*, 181–193. [CrossRef]
16. Su, H.-M.; Jiang, S.-Y.; Zhu, X.-Y.; Duan, Z.-P.; Huang, X.-K.; Zou, T. Magmatic-hydrothermal processes and controls on rare-metal enrichment of the Baerzhe peralkaline granitic pluton, inner Mongolia, northeastern China. *Ore Geol. Rev.* **2021**, *131*, 103984. [CrossRef]
17. Kuzmin, M.; Yarmolyuk, V. Mantle plumes of Central Asia (Northeast Asia) and their role in forming endogenous deposits. *Russ. Geol. Geophys.* **2014**, *55*, 120–143. [CrossRef]
18. Mongush, A.A.; Lebedev, V.I.; Kovach, V.P.; Sal'nikova, E.B.; Druzhkova, E.K.; Yakovleva, S.Z.; Plotkina, Y.V.; Zagornaya, N.Y.; Travin, A.V.; Serov, P.A. The tectonomagmatic evolution of structure-lithologic complexes in the Tannu–Ola zone, Tuva, in the Late Vendian–Early Cambrian (from geochemical, Nd isotope, and geochronological data). *Russ. Geol. Geophys.* **2011**, *52*, 503–516. [CrossRef]
19. Rudnev, S.N.; Kovach, V.P.; Ponomarchuk, V.A. Vendian–Early Cambrian island-arc plagiogranitoid magmatism in the Altai–Sayan folded area and in the Lake Zone of western Mongolia (geochronological, geochemical, and isotope data). *Russ. Geol. Geophys.* **2013**, *54*, 1272–1287. [CrossRef]
20. Vetrov, E.; Chernykh, A.; Babin, G. Early Paleozoic Granitoid Magmatism in the East Tannu-Ola Sector of the Tuvinian Magmatic Belt: Geodynamic Setting, Age, and Metallogeny. *Russ. Geol. Geophys.* **2019**, *60*, 492–513. [CrossRef]

21. Vetrov, E.V.; Uvarov, A.N.; Vetrova, N.I.; Letnikov, F.A.; Vishnevskaya, I.A.; Zhimulev, F.I.; Andreeva, E.S.; Chervyakovskaya, M.V. Petrogenesis of Despen volcanogenic formations of the Middle-Late Ordovician volcano-plutonic association of the Tannuol Terrane (Southwest Tuva). *Russ. Geol. Geophys.* **2021**, *62*, 633–647. [CrossRef]
22. Vetrov, E.; De Grave, J.; Vetrova, N.; Zhimulev, F.; Nachtergaele, S.; Van Ranst, G.; Mikhailova, P. Tectonic History of the South Tannuol Fault Zone (Tuva Region of the Northern Central Asian Orogenic Belt, Russia): Constraints from Multi-Method Geochronology. *Minerals* **2020**, *10*, 56. [CrossRef]
23. Vorontsov, A.; Yarmolyuk, V.; Dril, S.; Ernst, R.; Perfilova, O.; Grinev, O.; Komaritsyna, T. Magmatism of the Devonian Altai-Sayan Rift System: Geological and geochemical evidence for diverse plume-lithosphere interactions. *Gondwana Res.* **2020**, *89*, 193–219. [CrossRef]
24. Kozakov, I.K.; Didenko, A.N.; Azimov, P.Y.; Kirnozova, T.I.; Sal'Nikova, E.B.; Anisimova, I.V.; Erdenejargal, C. Geodynamic settings and formation conditions of crystalline complexes in the south Altai and south Gobi metamorphic belts. *Geotectonics* **2011**, *45*, 174–194. [CrossRef]
25. Kuzmin, M.I.; Yarmolyuk, V.V. Plate tectonics andmantle plumes as a basis of deepseated Earth's tectonic activity for the last 2 Ga. *Russ. Geol. Geophys.* **2014**, *55*, 120–143. [CrossRef]
26. Sugorakova, A.M.; Nikiforov, A.V. Basic magmatism of Early Devonian rifting Tuvinian trough. *Geosphere Res.* **2016**, *1*, 85–103. [CrossRef]
27. Yarmolyuk, V.V.; Nikiforov, A.V.; Sal'Nikova, E.B.; Travin, A.V.; Kozlovskiy, A.; Kotov, A.B.; Shuriga, T.N.; Lykhin, D.A.; Lebedev, V.I.; Anisimova, I.V.; et al. Rare-metal granitoids of the Ulug-Tanzek deposit (Eastern Tyva): Age and tectonic setting. *Dokl. Earth Sci.* **2010**, *430*, 95–100. [CrossRef]
28. Yarmolyuk, V.V.; Lykhin, D.A.; Kozlovsky, A.; Nikiforov, A.V.; Travin, A.V. Composition, sources, and mechanisms of origin of rare-metal granitoids in the Late Paleozoic Eastern Sayan zone of alkaline magmatism: A case study of the Ulaan Tolgoi massif. *Petrology* **2016**, *24*, 477–496. [CrossRef]
29. Williams, I.S. U–Th–Pb Geochronology by IonMicroprobe. In *Applications of Microanalytical Techniques to Understanding Mineralizing Processes*; McKibben, M.A., Shanks, W.C., Ridley, W.I., Eds.; Society of Economic Geologists: Littleton, CO, USA, 1998; Volume 7, pp. 1–35.
30. Black, L.P.; Kamo, S.L.; Allen, C.M.; Aleinikoff, J.N.; Davis, D.W.; Korsch, R.J.; Foudoulis, C. TEMORA 1: A new zircon standard for U-Pb geochronology. *Chem. Geol.* **2003**, *200*, 155–170. [CrossRef]
31. Stacey, J.S.; Kramers, J.D. Approximation of terrestrial lead isotope evolution by a two-stage model. *Earth Planet. Sci. Lett.* **1975**, *26*, 207–221. [CrossRef]
32. Vermeesch, P. IsoplotR: A free and open toolbox for geochronology. *Geosci. Front.* **2018**, *9*, 1479–1493. [CrossRef]
33. Jenner, G.A.; Longerich, P.; Jackson, S.E.; Fryer, B.J. ICP-MS—A powerful tool for high-precision trace-element analysis in Earth sciences: Evidence from analysis of selected U.S.G.S. reference samples. *Chem. Geol.* **1990**, *83*, 133–148. [CrossRef]
34. Bogomolov, E.S.; Guseva, V.F.; Turchenko, S.I. Mantle origin of the Pana Tundra layered mafic intrusion: Evidence from Sm–Nd and Rb–Sr data. *Geochem. Int.* **2002**, *40*, 855–859.
35. Faure, G. *Principles of Isotope Geology*; John Wiley Sons Inc.: New York, NY, USA, 1986.
36. De Paolo, D.J.; Linn, A.M.; Schubert, G. The continental crust age distribution: Methods of determining mantle separation ages fromSm-Nd isotopic data and application to the southwestern United States. *J. Geophys. Res.* **1991**, *96*, 2071–2088. [CrossRef]
37. Belousova, E.; Griffin, W.; O'Reilly, S.Y.; Fisher, N. Igneous zircon: Trace element composition as an indicator of source rock type. *Contrib. Miner. Pet.* **2002**, *143*, 602–622. [CrossRef]
38. Collins, W.J.; Beams, S.D.; White, A.J.R.; Chappell, B.W. Nature and origin of A-type granites with particular reference to southeastern Australia. *Contrib. Miner. Pet.* **1982**, *80*, 189–200. [CrossRef]
39. Whalen, J.B.; Currie, K.L.; Chappell, B.W. A-type granites: Geochemical characteristics, discrimination and petrogenesis. *Contrib. Mineral. Petrol.* **1987**, *95*, 407–419. [CrossRef]
40. Frost, B.R.; Barnes, C.G.; Collins, W.J.; Arculus, R.J.; Ellis, D.J.; Frost, C.D. A Geochemical Classification for Granitic Rocks. *J. Pet.* **2001**, *42*, 2033–2048. [CrossRef]
41. Le Maitre, R.W.B.; Dudek, P.; Keller, A.; Lameyre, J.; Le Bas, J.; Sabine, M.J.; Zanettin, A.R. A classification of igneous rocks and glossary of terms: Recommendations of the International Union of Geological Sciences. *Subcomm. Syst. Igneous Rocks* **1989**, *552*, 3.
42. Maniar, P.D.; Piccoli, P.M. Tectonic discrimination of granitoids. *Geol. Soc. Am. Bull.* **1989**, *101*, 635–643. [CrossRef]
43. Watson, E.B.; Harrison, T.M. Zircon saturation revisited: Temperature and composition effects in a variety of crustal magma types. *Earth Planet. Sci. Lett.* **1983**, *64*, 295–304. [CrossRef]
44. Sun, S.S.; McDonough, W.F. Chemical and isotopic systematics of oceanic basalts: Implications for mantle composition and processes. In *Magmatism in the Ocean Basin*; Geological Society Special Publication: London, UK, 1989; Volume 42, pp. 313–345.
45. McDonough, W.F.; Sun, S.-S. The composition of the Earth. *Chem. Geol.* **1995**, *120*, 223–253. [CrossRef]
46. Pearce, J.A.; Harris, N.B.W.; Tindle, A.G. Trace Element Discrimination Diagrams for the Tectonic Interpretation of Granitic Rocks. *J. Pet.* **1984**, *25*, 956–983. [CrossRef]
47. Harris, N.B.W.; Pearce, J.A.; Tindle, A.G. Geochemical characteristics of collision-zone magmatism. In *Geological Society*; Special Publications: London, UK, 1986; Volume 19, pp. 67–81. [CrossRef]
48. Chappell, B.W.; White, A.J.R. Two constrasting granite types. *Pac. Geol.* **1974**, *8*, 173–174.

49. Miller, C.F.; McDowell, S.M.; Mapes, R.W. Hot and cold granites? Implications of zircon saturation temperatures and preservation of inheritance. *Geology* **2003**, *31*, 529–532. [CrossRef]
50. Jiang, Y.-H.; Jiang, S.-Y.; Dai, B.-Z.; Liao, S.-Y.; Zhao, K.-D.; Ling, H.-F. Middle to late Jurassic felsic and mafic magmatism in southern Hunan province, southeast China: Implications for a continental arc to rifting. *Lithos* **2009**, *107*, 185–204. [CrossRef]
51. Yang, J.; Wu, F.; Chung, S.; Wilde, S.A.; Chu, M. A hybrid origin for the Qianshan A-type granite, northeast China: Geochemical and Sr–Nd–Hf isotopic evidence. *Lithos* **2006**, *89*, 89–106. [CrossRef]
52. Zhao, K.D.; Jiang, S.Y.; Yang, S.Y.; Dai, B.Z.; Lu, J.J. Mineral chemistry, trace elements and Sr–Nd–Hf isotope geochemistry and petrogenesis of Cailing and Furong granites and mafic enclaves from the Qitianling batholith in the Shi-Hang zone, South China. *Gondwana Res.* **2012**, *22*, 310–324. [CrossRef]
53. Litvinovsky, B.A.; Jahn, B.M.; Zanvilevich, A.N.; Saunders, A.; Poulain, S.; Kuzmin, D.V.; Reichow, M.K.; Titov, A.V. Petrogenesis of syenite–granite suites from the Bryansky Complex (Transbaikalia, Russia): Implications for the origin of A-type granitoid magmas. *Chem. Geol.* **2002**, *189*, 105–133. [CrossRef]
54. Martin, R. A-type granites of crustal origin ultimately result from open-system fenitization-type reactions in an extensional environment. *Lithos* **2006**, *91*, 125–136. [CrossRef]
55. Saunders, A.D.; Storey, M.; Kent, R.W.; Norry, M.J. Consequences of plume-lithosphere interactions. In *Magmatism and the Causes of Continental Break-up*; Storey, B.C., Alabaster, T., Pankhurst, R.J., Eds.; Geological Society: London, UK, 1992; Volume 68, pp. 41–60. [CrossRef]
56. Lassiter, J.C.; DePaolo, D.J. Plume/Lithosphere Interaction in the Generation of Continental and Oceanic Flood Basalts: Chemical and Isotopic Constraints. *Geophys. Monogr. -Am. Geophys. Union* **2013**, *100*, 335–355. [CrossRef]
57. Wedepohl, K.H. The composition of the continental crust. *Geochim. et Cosmochim. Acta* **1995**, *59*, 1217–1232. [CrossRef]
58. Laurent, O.; Martin, H.; Moyen, J.F.; Doucelance, R. The diversity and evolution of late-Archean granitoids: Evidence for the onset of 'modern-style' plate tectonics between 3.0 and 2.5 Ga. *Lithos* **2014**, *205*, 208–235. [CrossRef]
59. Shellnutt, J.G.; Wang, C.Y.; Zhou, M.-F.; Yang, Y. Zircon Lu–Hf isotopic compositions of metaluminous and peralkaline A-type granitic plutons of the Emeishan large igneous province (SW China): Constraints on the mantle source. *J. Southeast Asian Earth Sci.* **2009**, *35*, 45–55. [CrossRef]
60. Rudnick, R.L.; Gao, S. Composition of the Continental Crust. In *Treatise on Geochemistry*; Rudnick, R.L., Holland, H.D., Turekian, K.K., Eds.; Elsevier: Amsterdam, The Netherlands, 2003; Volume 3, pp. 1–64.
61. Wilson, M. *Igneous Petrogenesis: A Global Tectonic Approach*; Unwyn Hyman: London, UK, 1989.
62. Zhang, X.; Zhao, G.; Eizenhöfer, P.R.; Sun, M.; Han, Y.; Hou, W.; Liu, D.; Wang, B.; Liu, Q.; Xu, B.; et al. Tectonic transition from Late Carboniferous subduction to Early Permian post-collisional extension in the Eastern Tianshan, NW China: Insights from geochronology and geochemistry of mafic–intermediate intrusions. *Lithos* **2016**, *256-257*, 269–281. [CrossRef]
63. Taylor, S.R.; McLennan, S.M. *The Continental Crust: Its Composition and Evolution: An Examination of the Geochemical Record Preserved in Sedimentary Rocks*; Blackwell Scientific: Oxford, UK, 1985.
64. Condie, K.C. Mantle Plumes and their Record in Earth History. Cambridge University Press: Cambridge, UK, 2001. [CrossRef]
65. Pearce, J.A. Geochemical fingerprinting of oceanic basalts with applications to ophiolite classification and the search for Archean oceanic crust. *Lithos* **2008**, *100*, 14–48. [CrossRef]
66. Altunkaynak, Ş.; Dilek, Y.; Genc, C.S.; Sunal, G.; Gertisser, R.; Furnes, H.; Foland, K.A.; Jing-Sui, Y. Spatial, temporal and geochemical evolution of Oligo-Miocene granitoid magamtism in wester Anatolia, Turkey. *Gondwana Res.* **2012**, *21*, 961–986. [CrossRef]
67. Bi, J.-H.; Ge, W.-C.; Yang, H.; Wang, Z.-H.; Tian, D.-X.; Liu, X.-W.; Xu, W.-L.; Xing, D.-H. Geochemistry of MORB and OIB in the Yuejinshan Complex, NE China: Implications for petrogenesis and tectonic setting. *J. Southeast Asian Earth Sci.* **2017**, *145*, 475–493. [CrossRef]
68. Li, X.H.; Chen, Z.G.; Liu, D.Y.; Li, W.X. Jurassic gabbro-granite-syentite suites from southern Jiangxi Province, SE China: Age, origin and tectonic significance. *Int. Geol. Rev.* **2003**, *45*, 898–921. [CrossRef]
69. Eby, G. The A-type granitoids: A review of their occurrence and chemical characteristics and speculations on their petrogenesis. *Lithos* **1990**, *26*, 115–134. [CrossRef]
70. Zhang, H.F.; Parrish, R.; Zhang, L.; Xu, W.C.; Yuan, H.L.; Gao, S.; Crowley, Q.G. A-type granite and adakitic magmatism association in Songpan-Ganzi fold belt, eastern Tibetan Plateau: Implication for lithospheric delamination. *Lithos* **2007**, *97*, 323–335. [CrossRef]
71. Davies, J.H.; Von Blanckenburg, F. Slab breakoff: Amodel of lithosphere detachment and its test in the magmatism and deformation of collisional orogens. *Earth Planet. Sci. Lett.* **1995**, *129*, 85–102. [CrossRef]
72. Altunkaynak, Ş. Collision-driven slab break offmagmatismin Northwestern Anatolia, Turkey. *J. Geol.* **2007**, *115*, 63–82. [CrossRef]
73. Kuzmin, M.I.; Yarmolyuk, V.V.; Kravchinsky, V.A. Phanerozoic hot spot traces and paleogeographic reconstructions of the Siberian continent based on interaction with the African large low shear velocity province. *Earth-Science Rev.* **2010**, *102*, 29–59. [CrossRef]
74. Ernst, R.E.; Rodygin, S.A.; Grinev, O.M. Age correlation of Large Igneous Provinces with Devonian biotic crises. *Glob. Planet. Chang.* **2019**, *185*, 103097. [CrossRef]